Monthly Notices
of the
ROYAL ASTRONOMICAL SOCIETY

MNRAS **495,** 321–337 (2020)
Advance Access publication 2020 May 4

doi:10.1093/mnras/staa1148

Binary deviations from single object astrometry

Zephyr Penoyre [1]★, Vasily Belokurov [1], N. Wyn Evans,[1] A. Everall[1] and S. E. Koposov [1,2,3]

[1]*Institute of Astronomy, University of Cambridge, Madingley Road, Cambridge CB3 0HA, UK*
[2]*McWilliams Center for Cosmology, Carnegie Mellon University, 5000 Forbes Ave, Pittsburgh, PA 15213, USA*
[3]*Kavli Institute for Cosmology, University of Cambridge, Madingley Road, Cambridge CB3 0HA, UK*

Accepted 2020 April 22. Received 2020 April 22; in original form 2020 March 12

ABSTRACT

Most binaries are undetected. Astrometric reductions of a system using the assumption that the object moves like a single point mass can be biased by unresolved binary stars. The discrepancy between the *centre of mass* of the system (which moves like a point mass) and the *centre of light* (which is what we observe) introduces additional motion. We explore the extent to which binary systems affect single object model fit to astrometric data. This tells us how observations are diluted by binaries and which systems cause the largest discrepancies – but it also allows us to make inferences about the binarity of populations based on observed astrometric error. By examining a sample of mock observations, we show that binaries with periods close to 1 yr can mimic parallax and thus bias distance measurements, while long-period binaries can introduce significant apparent proper motion. While these changes can soak up some of the error introduced by the binary, the total deviation from the best-fitting model can be translated into a lower limit on the on-sky separation of the pair. Throughout, we link these predictions to data from the *Gaia* satellite, while leaving the conclusions generalizable to other surveys.

Key words: methods: analytical – astrometry – parallaxes – proper motions – binaries: general.

1 INTRODUCTION

Around half of the solar-type stars are in binary systems (Duquennoy & Mayor 1991; Raghavan et al. 2010). Among more massive stars, the fraction is higher still (Sana et al. 2012; Duchêne & Kraus 2013). The number and properties of binaries tell us about the conditions needed for star formation (Shu, Adams & Lizano 1987; Bate, Bonnell & Price 1995; Bonnell, Bate & Zinnecker 1998), the properties of the discs in which they form, and their motions both in the dense stellar nursery and during their long life histories. Binarity can affect the formation of planets and the eventual fate of a star. Some of the most exotic objects in the Galaxy result from the evolution of binary systems – including cataclysmic variables, hot Jupiters, and type 1a supernova (Whelan & Iben 1973; Tutukov & Yungelson 1981; Webbink 1984). It is even possible for a bright binary star companion to tell us of the presence of a massive dark body, such as a cool white dwarf or a stellar mass black hole (Andrews, Breivik & Chatterjee 2019).

However, the number of known binaries is tiny compared to the total number of catalogued stars. By many metrics, a typical binary star appears indistinguishable from a single object. This means that most binaries on sky are still undetected, and the information that can be gleaned from them still ready to be reaped. However, it also means that, though they may not be detectable, any observation we make assuming all stars are singular will necessarily be contaminated by binaries.

Currently, we know of around a hundred thousand visual binaries (Hartman & Lépine 2020), in which both objects can be separately resolved. Eclipsing binaries, in which the system is by chance aligned such that one star partially occults the other, are numbered in the thousands (Prša et al. 2011; Kirk et al. 2016). Binary stars can also be spotted directly from spectra if the two components have markedly different spectra that cannot be easily fitted by a single star model (El-Badry et al. 2018). Accurate distance measurements can also allow us to identify overbright systems that can most easily be explained by a multiple-star system (Widmark, Leistedt & Hogg 2018). Finally, spectroscopic binaries, whose motion can be seen by measuring the shift in the radial velocities over an orbit, are growing in number, with many thousands now known (Price-Whelan et al. 2020). These probe close binary pairs (generally with periods of 1 yr or less), for which multiple periods can be observed and which cause measurably large radial velocity shifts. Each of these methods is sensitive to different types of system, depending on distance, period, or stellar parameters – but in many systems multiple methods may be applicable helping to further constrain the properties.

★ E-mail: zephyrpenoyre@gmail.com

Instruments like *Hipparcos* (Perryman et al. 1997) and *Gaia* (Gaia Collaboration 2016) measure the position of stars on sky to very high accuracy and enable the discovery of astrometric binaries. These show significant binary motion on sky, on top of the motion of the centre of mass (c.o.m.), and are becoming detectable as the noise floor of astrometric observations reaches milliarcseconds (mas) precision (Gaia Collaboration 2018). Long-period systems will cause an extra component of motion of the c.o.m., changing slightly over time, termed a proper motion anomaly (Kervella et al. 2019), which is sensitive to relatively long-period binaries (around 10 yr or more).

In this paper, we focus on another way in which binarity can impinge on astrometric measurements: as excess error on a single-body astrometric fit. For systems with periods less than ∼10 yr, a significant ($\gtrsim$1/2) number of orbits can be completed over the observing period of a single instrument. Thus, we expect the astrometric motion of the c.o.m. to be well captured, but the binary motion to cause excess noise, which could potentially be harvested as inferred properties of the stars. By examining the analytic deviations in an ideal case (Section 2), we can make predictions which we then compare to a fuller numerical model (Section 3) and mock observations (Section 4). We can then gain insight into when the analytic treatment is accurate, and for which types of systems we expect a significant deviation. Finally, in Section 5, we discuss the impact of these effects on observable properties, both as an identifier of binary systems and a nuisance signal.

This analysis is heavily motivated by the *Gaia* survey, a space-based telescope measuring the position and velocities of millions of stars at a precision of a few mas over a period of years. However, most of the behaviour is general, and could be applied to surveys before and after *Gaia*. Thus, we will attempt to remain general, and invoke the properties of the *Gaia* survey only when fiducial numerical values are needed to further explore the results.

2 ANALYTIC DEVIATIONS

In the limit that the period of a binary is $\lesssim$ the observing time of a survey, we can derive an accurate analytic description of the magnitude of on-sky deviation between the movement of the centre of light (c.o.l.) compared to the c.o.m.

2.1 Offset between the centre of mass and of light

Let us start with a binary system, in which we label the bodies A and B. We assume that A is the more luminous of the two. Thus, we can remap the brightnesses of the two objects on to an absolute luminosity and a ratio such that $L = L_A$ and $l = L_B/L_A$. The total luminosity is $L_A + L_B = L(1 + l)$ with $l < 1$. We can define the mass similarly, with $M = M_A$ and $q = M_B/M_A$, which can be less than or greater than one. For a value significantly greater than one, the system can be described in the simpler framework of a massive dark companion (Shahaf et al. 2019).

When we do not spatially resolve a binary or – to be more precise – we cannot separate the point spread function (PSF) of the two sources, we see the system at the position of its c.o.l. However, the dynamics of the system govern the motion of the c.o.m. and thus if these two are offset, the c.o.l. will orbit around the c.o.m. causing the system to appear to be moving non-inertially.

If the total distance between the two sources is d, then the distance from A to the c.o.m. is $dq/(1 + q)$ while the distance to the c.o.l. is $dl/(1 + l)$.[1] Thus, if δd is the physical distance between the two, the fraction of the distance between the c.o.m. and the c.o.l. is

$$\Delta = \frac{\delta d}{d} = \frac{|q - l|}{(1 + q)(1 + l)}. \tag{1}$$

2.2 Two-body orbits

Assuming Keplerian potentials and no external forces, the orbit follows the usual parametric form. Using the eccentric anomaly η, the evolution of the separation d with time t is

$$d = a(1 - e\cos\eta), \qquad t = \frac{P}{2\pi}(\eta - e\sin\eta). \tag{2}$$

The orbital phase ϕ satisfies

$$\cos\phi = \frac{\cos\eta - e}{1 - e\cos\eta} \qquad \sin\phi = \frac{\sqrt{1 - e^2}\sin\eta}{1 - e\cos\eta}. \tag{3}$$

The semimajor axis a and period P are

$$a = -\frac{qGM^2}{2E}, \qquad \frac{P}{2\pi} = \sqrt{\frac{a^3}{(1 + q)GM}}, \tag{4}$$

and thus specifying M and q and either of a or T is sufficient to calculate the other. The eccentricity is

$$e^2 = 1 - \frac{1 + q}{q^2}\frac{L^2}{GM^3a}. \tag{5}$$

Here $E(< 0)$ and L are the total energy and angular momentum of the two bodies, respectively, and are constant over the orbit. We cannot solve equation (2) directly for $r(t)$, though approximate solutions are possible (Penoyre & Sandford 2019).

2.3 On-sky projection

It will be useful to work in spherical coordinates (r, θ, ϕ), where θ is the polar angle ranging from 0 to π and ϕ is the azimuthal angle ranging from 0 to 2π. We are free to set the orientation and thus align it with the phase of the binary at periapse (thus, making ϕ both the orbital phase and the azimuthal coordinate) and the origin is at the c.o.m. of the binary.

The two components of the binary lie in the $\pm\hat{\mathbf{d}}$ directions, where

$$\hat{\mathbf{d}} = \begin{pmatrix} \cos\phi \\ \sin\phi \\ 0 \end{pmatrix} \tag{6}$$

in Cartesian coordinates.

We can also define the position of an observer in this frame by two angles θ_v (equivalent to inclination, i) and ϕ_v such that the vector pointing towards the observer along the line of sight is

$$\hat{\mathbf{l}} = \begin{pmatrix} \cos\phi_v\sin\theta_v \\ \sin\phi_v\sin\theta_v \\ \cos\theta_v \end{pmatrix}. \tag{7}$$

Fig. 1 is a sketch of the system and the coordinates used, which we must transform to an on-sky projection and eventually to a motion in a specific coordinate frame (e.g. ecliptic longitude and latitude or RA and Dec).

[1]This is derived and explored in more detail in Appendix A.

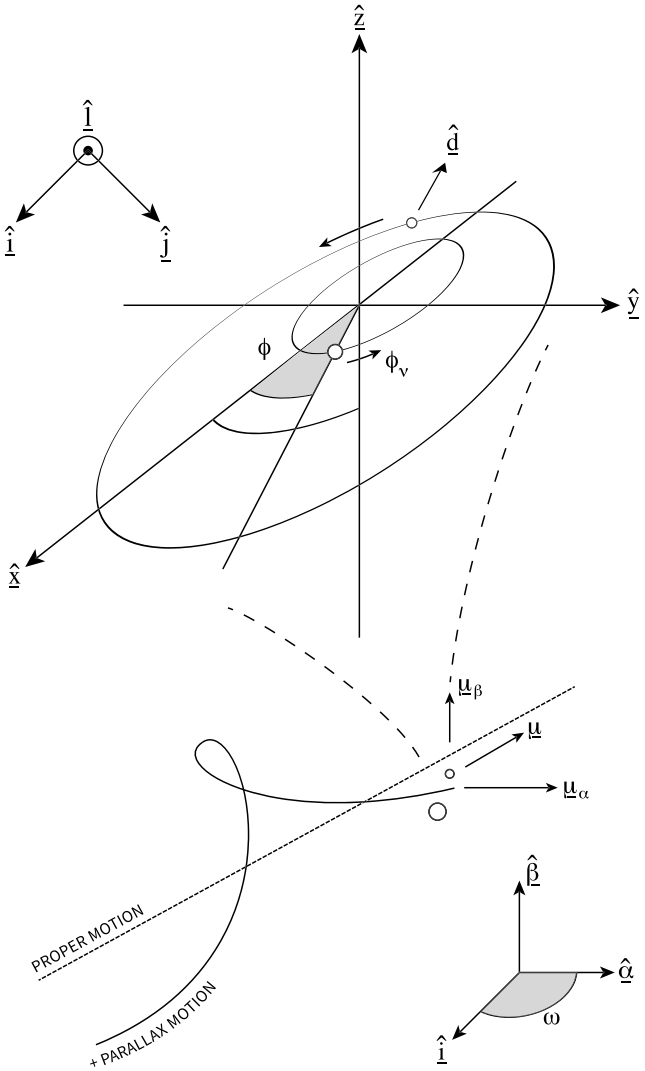

Figure 1. Sketch of the coordinate systems used to describe the motion of the binary and the centre of mass. Both views are shown as they would appear on sky (if the system could be resolved). Upper panel: Binary motion around the centre of mass (at the origin) as described in (x, y, z) coordinates with the orbit confined to the (x, y) plane and periapse of the brighter source on the x-axis. The azimuthal viewing angle ϕ_v is shown, while the polar viewing angle θ_v cannot be, as it is the angle between the vectors $\hat{\mathbf{z}}$ and $\hat{\mathbf{l}}$. The orbital phase of the binary is given by ϕ, and the phase relative to the viewing angle is $\varphi_v = \phi - \phi_v$ (if shown in this diagram it would be almost 2π). The centre of light will sit on the line between the two stars, at a constant fraction of the distance. To convert into on-sky motion, we project along the $\hat{\mathbf{i}}, \hat{\mathbf{j}}, \hat{\mathbf{l}}$ directions that lie in, and perpendicular to, the plane of the page. Bottom panel: The motion of the centre of mass of the system follows a straight line proper motion across the sky, with added motion caused by parallax (the change of a nearby object's position compared to the background due to Earth's orbit around the Sun). The final coordinate conversion is from on-sky coordinates with arbitrary direction specified by ω to those which line up with our reference coordinate system (e.g. ecliptic longitude and latitude or RA and Dec).

2.4 Deviations for a circular binary orbit

In the case of a circular orbit, the formulae thus presented are sufficient to describe the deviations caused by the binary. The magnitude of the projected binary separation is

$$|s| = d|\hat{\mathbf{l}} \wedge \hat{\mathbf{d}}| = d\sqrt{1 - \sin^2\theta_v(1 - \sin^2\varphi_v)}, \tag{8}$$

where $\varphi_v = \phi - \phi_v$ is the azimuthal angle between the orbital phase and the line-of-sight vector.

Let $\boldsymbol{\epsilon}$ be the 2D deviations of the c.o.l. from c.o.m. in on-sky coordinates – where we will express this here as an angle by multiplying through by the parallax of the object ϖ (this assumes that a is expressed in AU and thus ϵ has the same units as ϖ). The physical distance, projected perpendicular to the line of sight, between the c.o.m. and c.o.l. is thus

$$\begin{aligned}|\boldsymbol{\epsilon}| &= \Delta\varpi|s| \\ &= \frac{\varpi a|q-l|}{(1+q)(1+l)}\frac{1-e^2}{1+e\cos\phi}\sqrt{1-\sin^2\theta_v(1-\sin^2\varphi_v)}.\end{aligned} \tag{9}$$

Assuming that many periods of the binary are observed, the inferred astrometric scatter of a single-body fit is equal to

$$\delta\theta = \sqrt{\langle|\boldsymbol{\epsilon} - \langle\boldsymbol{\epsilon}\rangle|^2\rangle} = \sqrt{\langle|\boldsymbol{\epsilon}|^2\rangle - |\langle\boldsymbol{\epsilon}\rangle|^2}, \tag{10}$$

where $\langle\rangle$ denotes the time average. If we assume that a sufficient number of orbits occur over the observing period, we can take this average to be over a single complete orbit. For the circular case $\langle\boldsymbol{\epsilon}\rangle$ is zero, i.e. the average position of the object is at the foci, and thus

$$\delta\theta_{\rm circ} = \sqrt{\langle|\boldsymbol{\epsilon}|^2\rangle} = \frac{\varpi a|q-l|}{(1+q)(1+l)}\sqrt{1-\frac{\sin^2\theta_v}{2}}. \tag{11}$$

For non-circular orbits, $\langle\boldsymbol{\epsilon}\rangle$ is not in general zero and thus we must express the position on sky fully to calculate δ.

2.5 Binary motion across the sky plane

As illustrated in Fig. 1, it is natural to define two other unit vectors that capture the projection on the plane perpendicular to $\hat{\mathbf{l}}$ (and thus describe the position on sky). These vectors can be taken as

$$\hat{\mathbf{i}} = \frac{1}{\sqrt{1-\sin^2\theta_v\cos^2\phi_v}}\begin{pmatrix}1-\cos^2\phi_v\sin^2\theta_v\\ -\sin\phi_v\cos\phi_v\sin^2\theta_v\\ -\cos\phi_v\sin\theta_v\cos\theta_v\end{pmatrix}, \tag{12}$$

which projects on to the x-axis and thus appears to pass through the orbital periapse and apoapse and

$$\hat{\mathbf{j}} = \frac{1}{\sqrt{1-\sin^2\theta_v\cos^2\phi_v}}\begin{pmatrix}0\\ \cos\theta_v\\ -\sin\phi_v\sin\theta_v\end{pmatrix}, \tag{13}$$

which completes the orthonormal set. The choice of these two directions is arbitrary (at least until we define the orientation of the system on the sky), but provides an easily interpretable coordinate system.

In these coordinates, the c.o.l. at time t is at position

$$\begin{aligned}i &= \Delta(\hat{\mathbf{i}}\cdot\mathbf{d}) = \frac{\Delta a(1-e^2)}{1+e\cos\phi}\frac{\cos\phi - \cos\varphi_v\cos\phi_v\sin^2\theta_v}{\sqrt{1-\sin^2\theta_v\cos^2\phi_v}},\\ j &= \Delta(\hat{\mathbf{j}}\cdot\mathbf{d}) = \frac{\Delta a(1-e^2)}{1+e\cos\phi}\frac{\sin\phi\cos\theta_v}{\sqrt{1-\sin^2\theta_v\cos^2\phi_v}},\\ l &= \Delta(\hat{\mathbf{l}}\cdot\mathbf{d}) = \frac{\Delta a(1-e^2)}{1+e\cos\phi}\cos\varphi_v\sin\theta_v\end{aligned} \tag{14}$$

where $\varphi_v = \phi - \phi_v$ is the azimuthal angle between the current position and the line of sight and $\mathbf{d}$ is specified by equations (2) and (6).

Thus, at any given time, the full on-sky deviation from the c.o.l. to c.o.m. is given by

$$\boldsymbol{\epsilon} = \varpi\begin{pmatrix}i\\ j\end{pmatrix}. \tag{15}$$

Taking the time average of this, we find

$$\langle \boldsymbol{\epsilon} \rangle = -\frac{3e\varpi|q-l|a}{2(1+q)(1+l)}\sqrt{1-\cos^2\phi_v \sin^2\theta_v}\begin{pmatrix}1\\0\end{pmatrix} \tag{16}$$

and thus the full expression for $\delta\theta$ given any eccentricity is

$$\delta\theta = \frac{\varpi a|q-l|}{(1+q)(1+l)}\sqrt{1-\frac{\sin^2\theta_v}{2}-\frac{3+\sin^2\theta_v(\cos^2\phi_v-2)}{4}e^2}. \tag{17}$$

In the circular limit, this agrees with the expression in equation (11) as expected. For orbits approaching radial, we find

$$\delta\theta_{\rm rad} = \frac{\varpi a|q-l|}{2(1+q)(1+l)}\sqrt{1-\cos^2\phi_v \sin^2\theta_v}. \tag{18}$$

Inspection of equation (17) shows that eccentricity always decreases $\delta\theta$.

In Appendix B, we derive a comprehensive, but significantly more complex, expression for the full behaviour.

2.6 Binary motion as astrometric error

If we do not resolve a binary and fit it as a single source, this on-sky motion of the c.o.l. behaves as a source of astrometric error in two ways.

First, it may change the inferred astrometric parameters. Significant motion due to a binary could be interpreted as a change in the motion of a single point source. Long-period binaries will have a roughly constant offset from the c.o.m. Intermediate-period systems, which complete a significant fraction of one orbit over the observing time, can mimic significant proper motion. We investigate this in detail for our numerical models in Section 3. Secondly, the motion of systems with periods close to 1 yr may mimic parallactic motion, and thus bias our estimate of the distance. Thirdly, it may increase the observed noise. For systems for which the astrometric fit to the c.o.l. motion well matches the c.o.m. motion, any on-sky deviations appear as additional noise. Thus, systems with anomalously high inferred noise may be caused by binaries – and conversely high observed noise can be translated to a prediction of binary properties.

Apparent motion of a single star on the sky, though it has five free parameters, is highly constrained – consisting of straight line motion across the sky superimposed on the apparent motion of nearby sources due to Earth's orbit around the Sun. The form of the latter is fixed by the source position on sky, with the parallax only scaling the magnitude of the effect. Thus, it is hard, though far from impossible (especially in huge data sets such as the *Gaia* survey), to convincingly mimic astrometric motion with short-period binaries. Thus, binary motion will mostly contribute to increased error in these cases.

Any observation also has some intrinsic astrometric error, $\sigma_{\rm ast}$ (which is in part a function of the source, but we shall take as constant for a given instrument). When we fit an astrometric model on to a single source, we can construct the statistic

$$\chi^2 = \sum^{N_{\rm obs}}\left(\frac{(\alpha_{\rm obs}-\alpha_{\rm model})^2+(\beta_{\rm obs}-\beta_{\rm model})^2}{\sigma_{\rm ast}^2}\right). \tag{19}$$

Here α and β are the on-sky angular coordinates and $N_{\rm obs}$ is the number of observations of the source. For a single star, we would expect this to be close in value to $\sim N_{\rm obs}-5$, where the five corresponds to the degrees of freedom of the astrometric fit.

When we add the induced motion of a binary, we expect the χ^2 to increase by $\chi^2_{\rm binary} = \delta\theta^2/\sigma^2_{\rm ast}$ from which we can make a prediction of the Unit Weight Error (UWE)

$$\mathrm{UWE}_{\rm pred} = \sqrt{\frac{\chi^2_{\rm total}}{N_{\rm obs}-5}} \simeq \sqrt{1+\left(\frac{\delta\theta}{\sigma_{\rm ast}}\right)^2} \tag{20}$$

(ignoring cross-terms). This is a parameter recorded by the *Gaia* survey, in the form of Renormalized Unit Weight Error (RUWE) rescaling to account for systematic trends in the measurements[2] and thus can be used to explore the distribution of binaries across the huge *Gaia* DR2 catalogue (Belokurov et al. 2020).

3 NUMERICAL DEVIATIONS

For systems with longer periods, or those inhabiting certain (un)fortunate parts of parameter space, the presence of a binary companion biases the astrometric fit, such that the inferred parallax, position, and proper motion are inaccurate. These cases defy easy analytical exploration, but can be modelled numerically. By fitting single-body astrometric solutions to their more complex on-sky motion, we can compare the accuracy and precision of our astrometric fits as a function of the properties of the binary.

3.1 Path of the c.o.m.

Given the above tools, we map out the path across the sky of the c.o.l. of a binary system – combining the on-sky motion of the c.o.m. and the c.o.l. The former moves as a single body, including the effects of parallax, and can travel a non-negligible distance on sky over the observing period. The latter is a correction to this motion capturing the Keplerian binary orbit, and can be assumed to be sufficiently small such that the orbit is constant over the observing period (i.e. the parameters of the orbit, including viewing angles, are constant) and can be modelled as a linear correction to the c.o.m. position.

The single body motion depends on the orbit of the Earth, and the position and proper motion. The most natural coordinate system to use is the ecliptic, as it is the Earth's motion around the Sun that traces the parallactic ellipse. Letting $\phi_{\rm E}$ be the phase of Earth's orbit and $e_{\rm E}$ the eccentricity, we can express the full single-body astrometric motion as

$$\begin{aligned}\Delta\alpha(t) = {}& \Delta\alpha_0 + (t-t_0-t_{\rm b})\mu_\alpha \\ & - \frac{\varpi}{\cos\beta_i}(\cos\psi + e_{\rm E}(\sin\psi\sin\tau - \cos\phi))\end{aligned} \tag{21}$$

and

$$\begin{aligned}\Delta\beta(t) = {}& \Delta\beta_0 + (t-t_0-t_{\rm b})\mu_\beta \\ & - \varpi\sin\beta_i(\sin\psi + e_{\rm E}(\cos\psi\sin\tau + \sin\phi)),\end{aligned} \tag{22}$$

where

$$t_{\rm b} = \frac{A_u\cos\beta_i}{c}(\cos\psi - \cos\psi_0 + e_{\rm E}(\sin\tau\sin\psi - \sin\tau_0\cos\psi_0)), \tag{23}$$

$\psi(t) = \phi_{\rm E}(t) - \tau$ and $\tau = \frac{2\pi(t-t_{\rm p})}{T_{\rm E}}$, where $T_{\rm E}$ is 1 yr and $t_{\rm p}$ is the time of any pericentre passage of the Earth.[3] These results are derived in detail in Appendix C.

[2] See the *Gaia* consortium's technical note GAIA-C3-TN-LU-LL-124-01.
[3] For example, in relevance to *Gaia* we might use $t_{\rm p} = 2456662.00$ BJD, shortly before the beginning of astrometric observations in *Gaia* DR2, $t_0 = 2456863.94$ BJD.

3.2 Path of the c.o.l.

As the binary separations are always small (compared to angles spanning the whole sky), the addition of the binary component is approximately linear.

Section 2.5 has mapped out the contribution due to the binary orbit, but one final transformation must be made to align the orientation of the binary system with our on-sky coordinates of choice. We could imagine taking the system shown in Fig. 1 and putting a pin through the origin, along the line of sight, and then rotating the page beneath that pin. This introduces one last viewing angle, the orientation of the system relative to our reference axes, ω_v. We can also at this point move from coordinates describing physical distances to movements on sky by multiplying by the parallax, ϖ, (as a is given in AU) to give the deviations of the c.o.l. in the azimuthal and polar coordinates of our chosen astronomical system (α_b, β_b):

$$\alpha_b = \varpi(i\cos\omega_v + j\sin\omega_v) \text{ and } \beta_b = \varpi(\cos\omega_v j - \sin\omega_v i). \tag{24}$$

Thus, adding equations (21), (22), and (24), we can describe the motion of the c.o.l. as observed by a survey such as *Gaia*. Examples of such motions are shown for eight mock observations in Fig. 2, as detailed in the next section.

4 MOCK OBSERVATIONS

We can generate mock observations by calculating the position of the c.o.l. at a series of times. For significant binary separations, this will deviate from the single-body orbit; thus, it is of interest to ask how well we might fit a single-body orbit to the observed path and how far our fit may be from the true parameters.

As an exploratory exercise, we have done this for two million systems, for which we have chosen the parameters of the binary based on the distributions listed in Table 1. For simplicity, we work in coordinates aligned with the ecliptic plane, though as long as we are consistent we are free to use any angular coordinate system.

The distributions of these parameters have been chosen to be both qualitatively representative of real data and relatively simple. In some places, a balance has been struck between the two. For example, the distributions of ϖ, μ_α, and μ_β are taken from simple fits to one million random *Gaia* sources (with parallax over error greater than 15), while the angular positions are chosen to be uniform on sky – whereas in reality stars are much more clustered in the plane of the Milky Way and towards the Galactic Centre. As the equations describing on-sky motion are approximately linear in parallax and proper motion, the actual value should have little impact on the offset (the value of interest).

The masses of the brightest star are taken from an initial mass function proportional to $M^{-2.3}$, limited to stars above $0.5\,\mathrm{M}_\odot$ (a range in which most IMFs converge). We initially experimented with an empirical period distribution of binaries from Raghavan et al. (2010), though this peaks at a period of ∼100 yr, at which binary motion is negligible within *Gaia*'s temporal baseline (and also orbital separation is large enough that the sources may be independently resolvable depending on parallax). Instead, we limited our period to 10 yr (effectively restricting the binary separation to a few mas for our parallax distribution), and chose a distribution that favours short periods and resembles the Raghavan et al. (2010) distribution if curtailed at 10 yr, a range containing around 20 per cent of all binaries. For simplicity, we use a uniform distribution of luminosity ratios. In general, we expect luminosity and mass ratio to correlate so, to (very loosely) represent this, we choose a value of q log-normally distributed around l. Thus, q will generally be close in value to l, but also tend to be slightly larger (luminosity normally scales strongly with mass) and have a wide spread that can encompass dark-massive companions and low-mass bright giants. The eccentricity was chosen to produce more circular orbits than highly eccentric ones. Finally, t_0, θ_v, ϕ_v, and ω_v are all parameters we expect to be isotropic.

The sample of generated systems is intended to represent actual systems only in a loose sense – the focus being on spanning the parameter space with a sensible distribution, not on recovering detailed statistics of actual binaries. If we were really inclined to scale up the proportion of binaries of these properties to the whole sample of observed stars in a survey such as *Gaia*, it would be contingent on estimating the fraction of all stars that are unresolved binaries with periods less than 10 yr. We expect other significant sources of error to be the choice of distributions of l and q (which are chosen for numerical convenience not based on physics or observations), which may cause over/underabundances of some types of systems but are unlikely to change bulk properties.

For each system, we calculate the position of the c.o.l. at 100 times, randomly spaced over a 22 month period (a rough approximation to the *Gaia* survey) – with an added astrometric error of $\sigma_{\mathrm{ast}} = 0.2$ mas, distributed isotropically on sky. To simulate observations, we fit single-body astrometric solutions to the sample of generated mock observations, and via linear least squares, we find best fits and errors on $\Delta\alpha_0$, $\Delta\beta_0$, μ_α, μ_β, and ϖ (details of these fits are given in Appendix D).

4.1 Results from mock observations

Fig. 2 shows a sample of eight astrometric mock observations, including their parameters. The first five have binary periods less than the observing time of 22 months, while the last three have longer periods. All systems shown have significant binary motions, and many show substantial deviation from their c.o.m. motion. However, not all of them have large UWE, as variation, particularly in proper motion, can mimic the effect of the binary at long periods, and at short periods binary deviations can act as extra astrometric noise and just increase variance in the astrometric fit.

Some binary motion is not easily approximated by parallactic motion – in the first example in Fig. 2, a binary period of just under half a year gives a smooth well-behaved curve, but one impossible to fit well with a single-body astrometric fit. The third example is one of a small but significant minority in which binary motion at a period close to 1 yr enlarges (or in other cases contracts) the parallax ellipse and changes the inferred parallax significantly. At the same time, some binaries with long periods and large on-sky deviations are fitted very well by the model, which translates their on-sky motion to erroneous proper motion.

4.2 Distribution of binary deviations

The parameter space over which we have sampled binaries is large (12 dimensional). For real observations, it could feasibly be even larger, including information about scanning laws and variable errors. Thus, the only conclusions we can draw from the mock data are about the large-scale distributions, particularly

about the magnitude of departures from the true astrometric solution for the c.o.m. motion and how this depends on binary parameters.

In Fig. 3, we compare the period of binaries to the shift in inferred parallax, $\Delta\varpi = \varpi - \varpi_{\rm true}$, total proper motion, $|\Delta\mu| = \sqrt{(\mu_\alpha - \mu_{\alpha,\rm true})^2 + (\mu_\beta - \mu_{\beta,\rm true})^2}$, and the goodness of fit as characterized by observed UWE (equation 20). We show the number density of all our mock observations (top row), and the distribution compared with reference to $\delta\theta$ (bottom row) – a close proxy for the magnitude of the contribution of the binary.

Starting in the left-hand column, we see that the vast majority of systems have small and likely imperceptible parallax deviations, but some can be shifted by 1 mas or more. As we might expect, parallax shift is only significant for systems with periods close to 1 yr, a relationship that would likely become tighter for a longer observing period. Those systems with large $|\Delta\varpi|$ tend to have a significant binary component ($\delta\theta \sim 1$ mas), but it is not the case that the most extreme binaries give the largest shift.

Unlike the parallax, the proper motion deviations (middle column) can be large ($\lessapprox 10$ mas yr^{-1}) for any period longer than about 1 yr, and the most extreme binaries tend to provide the largest $\Delta\mu$. Finally, the UWE (right-hand column) also peaks at periods close to 1 yr, but can be significant in systems with any but the smallest period (note, however, that short-period systems at small distances can provide significant UWE but are lacking in our mock sample). For a fixed period, higher $\delta\theta$ corresponds to higher UWE. Few systems at 10 yr periods have significant UWE, but there it is clear that UWE > 2 can still occur even in systems with $P > 10$ yr.

UWE scales linearly with parallax – and thus closer systems can have significantly larger values. The highest parallaxes used in the mock observations are around 10 mas. For systems in the local

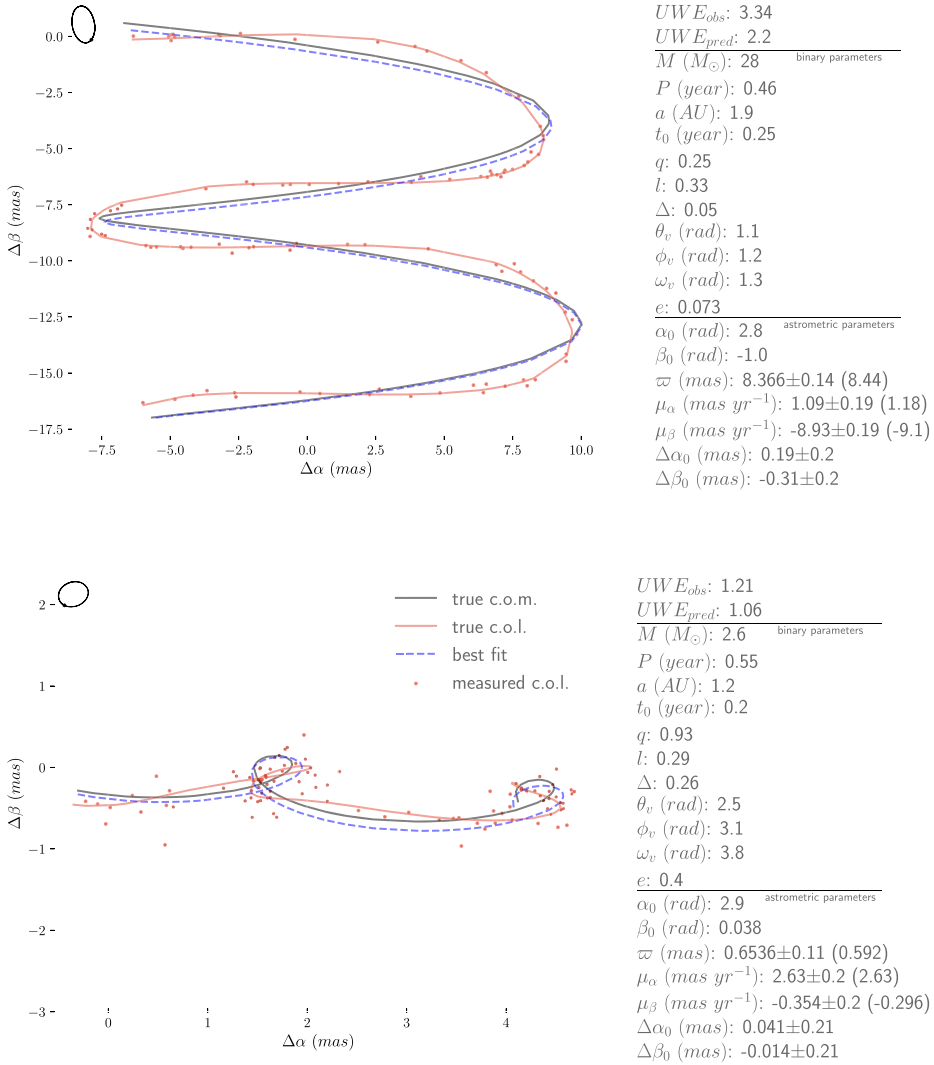

Figure 2. Eight example unresolved binaries, showing: the motion of the centre of mass (black line) that moves as a single body, the motion of the centre of light (red line) that deviates due to binarity, and the simulated observations including error that we fit to (red dots). The best-fitting single body curve is also shown (dashed blue). Also shown in the top left is the ellipse (or fraction thereof) traced by the centre of light excluding parallax motion – to the same scale. The properties of each system are shown to the right of the plots. Values derived from the least-squares fit are given with errors (true values in brackets). 1000 such fits can be viewed here.

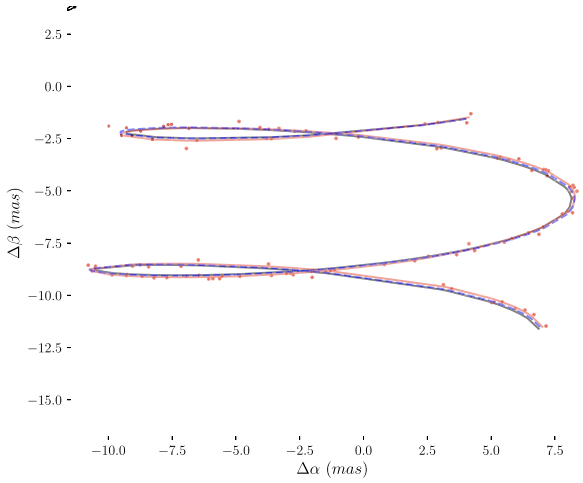

UWE_{obs}: 1.16
UWE_{pred}: 1.01
M $(M_\odot)$: 2.8 (binary parameters)
P $(year)$: 0.87
a (AU): 1.3
t_0 $(year)$: 0.09
q: 0.094
l: 0.24
Δ: 0.11
θ_v (rad): 1.9
ϕ_v (rad): 3.3
ω_v (rad): 3.7
e: 0.37
α_0 (rad): 6.3 (astrometric parameters)
β_0 (rad): 1.2
ϖ (mas): 1.572±0.024 (1.54)
μ_α $(mas\ yr^{-1})$: -1.18±0.21 (-1.19)
μ_β $(mas\ yr^{-1})$: -6.56±0.21 (-6.55)
$\Delta\alpha_0$ (mas): -0.058±0.23
$\Delta\beta_0$ (mas): 0.015±0.23

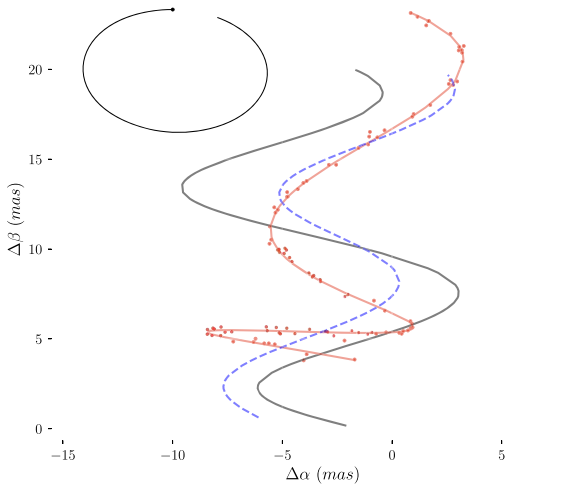

UWE_{obs}: 12.5
UWE_{pred}: 10.1
M $(M_\odot)$: 0.72 (binary parameters)
P $(year)$: 1.1
a (AU): 1.4
t_0 $(year)$: 0.59
q: 2.3
l: 0.17
Δ: 0.56
θ_v (rad): 0.62
ϕ_v (rad): 4.1
ω_v (rad): 2.8
e: 0.15
α_0 (rad): 6.1 (astrometric parameters)
β_0 (rad): 0.63
ϖ (mas): 3.339±0.14 (5.43)
μ_α $(mas\ yr^{-1})$: 2.54±0.2 (-3.47)
μ_β $(mas\ yr^{-1})$: 10.7±0.19 (11.1)
$\Delta\alpha_0$ (mas): -4.8±0.22
$\Delta\beta_0$ (mas): 0.49±0.2

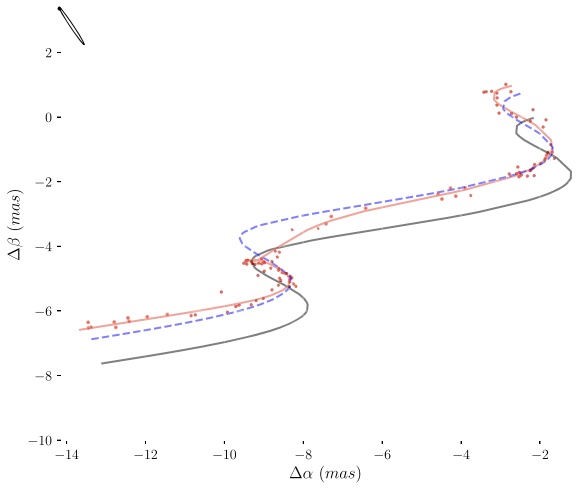

UWE_{obs}: 2.09
UWE_{pred}: 1.92
M $(M_\odot)$: 5.1 (binary parameters)
P $(year)$: 1.6
a (AU): 2.4
t_0 $(year)$: 1.1
q: 0.13
l: 0.32
Δ: 0.13
θ_v (rad): 1.7
ϕ_v (rad): 4.5
ω_v (rad): 4.2
e: 0.8
α_0 (rad): 0.27 (astrometric parameters)
β_0 (rad): 0.33
ϖ (mas): 2.049±0.15 (2.14)
μ_α $(mas\ yr^{-1})$: -6.66±0.19 (-6.68)
μ_β $(mas\ yr^{-1})$: -4.1±0.19 (-4.09)
$\Delta\alpha_0$ (mas): -0.41±0.21
$\Delta\beta_0$ (mas): 0.76±0.21

Figure 2 – *continued*

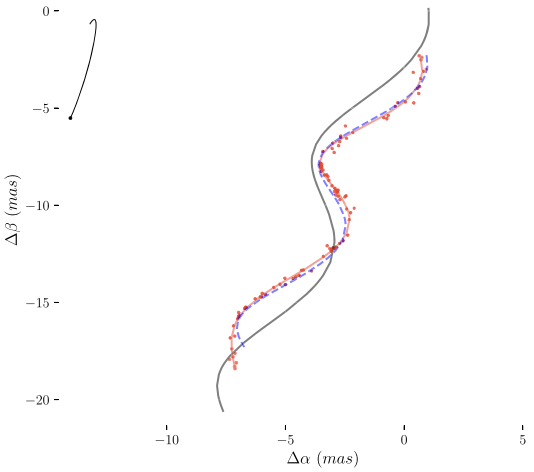

UWE_{obs}: 2.08
UWE_{pred}: 3.8
M $(M_\odot)$: 110 (binary parameters)
P $(year)$: 2.3
a (AU): 12
t_0 $(year)$: 2.1
q: 1.6
l: 0.73
Δ: 0.2
θ_v (rad): 1.5
ϕ_v (rad): 3.6
ω_v (rad): 4.8
e: 0.25
α_0 (rad): 3.0 (astrometric parameters)
β_0 (rad): 0.63
ϖ (mas): 1.333±0.15 (1.34)
μ_α $(mas\ yr^{-1})$: -3.44±0.21 (-3.99)
μ_β $(mas\ yr^{-1})$: -8.37±0.19 (-11.5)
$\Delta\alpha_0$ (mas): -0.083±0.22
$\Delta\beta_0$ (mas): -2.4±0.21

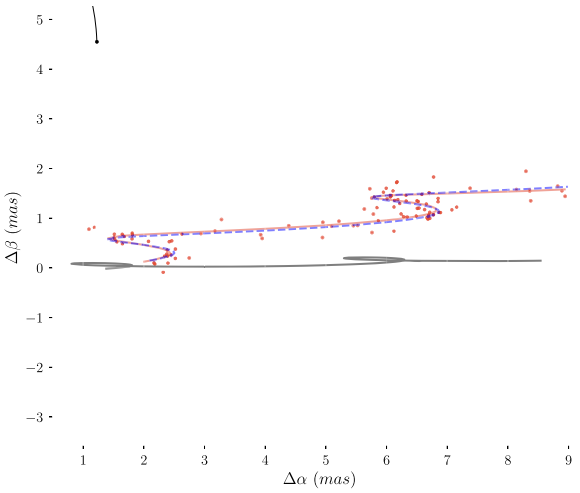

UWE_{obs}: 1.03
UWE_{pred}: 3.47
M $(M_\odot)$: 0.62 (binary parameters)
P $(year)$: 6.9
a (AU): 4.9
t_0 $(year)$: 4.7
q: 2.8
l: 0.85
Δ: 0.28
θ_v (rad): 1.3
ϕ_v (rad): 3.9
ω_v (rad): 4.4
e: 0.092
α_0 (rad): 3.2 (astrometric parameters)
β_0 (rad): 0.94
ϖ (mas): 1.446±0.15 (1.41)
μ_α $(mas\ yr^{-1})$: 4.36±0.2 (4.49)
μ_β $(mas\ yr^{-1})$: 0.84±0.19 (0.113)
$\Delta\alpha_0$ (mas): 0.68±0.23
$\Delta\beta_0$ (mas): 0.16±0.21

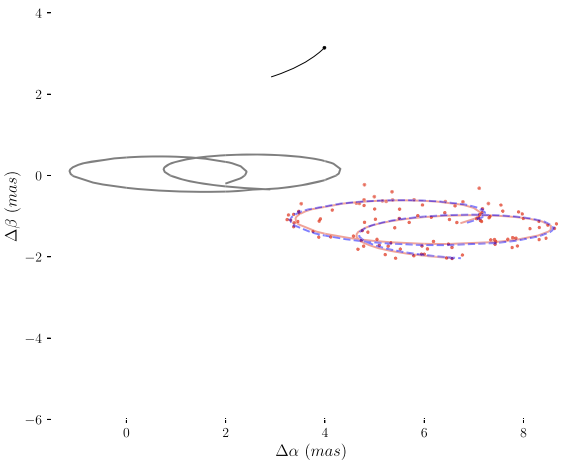

UWE_{obs}: 0.962
UWE_{pred}: 7.19
M $(M_\odot)$: 1.1 (binary parameters)
P $(year)$: 8.8
a (AU): 5.8
t_0 $(year)$: 6.5
q: 1.4
l: 0.48
Δ: 0.26
θ_v (rad): 2.3
ϕ_v (rad): 4.0
ω_v (rad): 3.3
e: 0.71
α_0 (rad): 1.6 (astrometric parameters)
β_0 (rad): -0.21
ϖ (mas): 2.235±0.15 (2.17)
μ_α $(mas\ yr^{-1})$: 1.38±0.2 (1.9)
μ_β $(mas\ yr^{-1})$: -0.356±0.19 (0.0476)
$\Delta\alpha_0$ (mas): 4.8±0.2
$\Delta\beta_0$ (mas): -0.96±0.2

Figure 2 – *continued*

Table 1. Parameters and distributions used to generate the mock observations. The first five define the single-body astrometric motion and the others define the binary motion. Here $U[a, b]$ represents a uniformly drawn random number between a and b, $N[\mu, \sigma]$ represents a number drawn from a normal distribution with mean μ and width σ, and $S[\mu, \sigma, \varsigma]$ is a draw from a split-normal distribution with mode μ, and width σ below the mode and ς above.

Variable	Description	Distribution
ϖ [mas]	Parallax	$10^{S[-0.05,\,0.17,\,0.36]}$
α_0 [rad]	Azimuthal position (t=0)	$2\pi \cdot U[0, 1]$
β_0 [rad]	Polar position (t=0)	$\sin^{-1}(U[-1, 1])$
μ_α [mas yr^{-1}]	Azimuthal proper motion	$N[-1.6, 7.6]$
μ_β [mas yr^{-1}]	Polar proper motion	$N[-3.0, 7.9]$
l	Binary luminosity ratio	$U[0, 1]$
q	Binary mass ratio	$l \cdot 10^{N[0,\,\frac{1}{2}]}$
P [yr]	Binary period	$10 \cdot U[0, 1]^2$
t_0	Time of binary periapse	$P \cdot U[0, 1]$
M [M$_\odot$]	Mass of bright companion	$\frac{1}{2}(1 - U[0, 1])^{-0.77}$
e	Binary eccentricity	$U[0, 1]^2$
θ_v [rad]	Polar viewing angle	$\cos^{-1}(U[-1, 1])$
ϕ_v [rad]	Azimuthal viewing angle	$2\pi \cdot U[0, 1]$
ω_v [rad]	Coord. projection angle	$2\pi \cdot U[0, 1]$

vicinity of the Sun, parallaxes could reach 100's of mas and thus for the same systems, the signal could be very large, or alternatively the magnitude of binary deviations could be an order of magnitude smaller and still detectable.

4.2.1 *Comparing to predicted UWE*

In Fig. 4, we compare the predicted UWE as calculated via the methods in Section 2.1 to that we find from fitting to the mock data. Looking at the number density, we see that the predicted UWE is effectively an upper limit on the observed UWE, with all systems falling on or below the 1:1 line. It is systems with low periods, peaking near 1 yr, for which the predictions and observations agree well (lower periods may still be accurate, but both the predicted and observed signals are very close to 1). As might be expected, closer objects (larger parallax) have larger predicted and observed UWE. For a given $\mathrm{UWE_{pred}}$, closer objects tend to have a higher $\mathrm{UWE_{obs}}$, which is a selection effect on period (for a fixed $\delta\theta$, further systems must be wider binaries).

The eccentricity distribution is relatively flat, but there are a few interesting features to note. Given the higher number of low-eccentricity orbits, we would expect these to dominate across the rest of the plot, but interestingly in the intermediate region ($1 < \mathrm{UWE_{obs}} < \mathrm{UWE_{pred}}$), we see an overdensity of eccentric systems. The reason for this is that the information content of an eccentric orbit is syncopated, and the slow motion around apoapse is about equally informative as the fast pericentre passage – thus, for long period orbits, the observed UWE can still be relatively high if the short observing window overlaps with pericentre passage. This is more clearly seen in Appendix E, where we separate this plot by period.

Well-predicted UWEs tend to have a higher $\Delta\varpi$, but this is mostly due to the fact that their orbital period distribution overlaps with 1 yr. More tellingly, the well-predicted orbits tend to have low $\Delta\mu$ – showing that the effect of the binary tends to either be represented in the UWE or in extra proper motion, but not both.

4.2.2 *Magnitude of deviations*

We have seen a few examples where the binary contribution can be 'absorbed' into the astrometric solution, and not show itself directly in UWE. In Fig. 5, we explore this by comparing the total deviation from the true parameters, weighted by their errors

$$\frac{\Delta\Sigma}{\sigma_\Sigma} = \sqrt{\left(\frac{\Delta\varpi}{\sigma_\varpi}\right)^2 + \left(\frac{\Delta\mu_\alpha}{\sigma_{\mu_\alpha}}\right)^2 + \left(\frac{\Delta\mu_\beta}{\sigma_{\mu_\beta}}\right)^2 + \left(\frac{\Delta\alpha_0}{\sigma_{\alpha_0}}\right)^2 + \left(\frac{\Delta\beta_0}{\sigma_{\beta_0}}\right)^2} \quad (25)$$

to the UWE. This quantity goes to zero along the 1:1 line in the plot, and thus systems on this line have most of their error dominated by *UWE*. When above the line, most of the total error is absorbed within the fit.

Comparing the first and second panels, we can see that the low-UWE ($\lessapprox$1.2) systems can be split into two major groups – short-period systems with smaller parameter error, and very long period binaries completely dominated by parameter error. Looking to the remainder of the middle panel, we see that intermediate-period systems vary greatly in the relative contribution of errors, but interestingly contours of constant period agree well with constant total error – i.e. the period is a good predictor of total error, but not whether it will be absorbed into the fit or the UWE. Finally, looking at the binary contribution, as described by $\delta\theta$, we see that both UWE and total error increase with more significant binaries.

This behaviour complicates the simple interpretation of a single object and what can be inferred from its UWE. The analytic prediction, working from an observation back to the properties of the binary, will give a lower limit on the size of the orbit/mass of the components – but depending on unseen factors that may be a lower limit by some small percentage or orders of magnitude. For a large population, this suggests that UWE will be a relatively robust measurement of binarity, though again an underestimate. It is possible that more information about the binary can be extracted by comparing to the covariance of errors in the parameter estimation (UWE being effectively the collapse of these variances and covariances to a single scalar quantity).

5 REAL OBSERVATIONS

The importance of these short-period binaries on astrometric observations can be split into two cases. In the first, they are a blessing, giving us a new method for identifying binary systems – imperfectly but potentially in huge numbers, or reliably across populations. In the second, they are a nuisance, biasing a small fraction of our sample with no clean or universal way to account or adjust for them.

5.1 Binary identification

For any observed astrometric system, we can measure the UWE. The question is then whether we can reliably convert this to an inference about the presence and properties of a possible binary.

Fig. 6 shows, as a function of the observed UWE of our mock observations, the true $\delta\theta$. There is a wide spread in $\delta\theta$ for any given UWE, but for higher UWE the majority of systems do lie along a relatively tight relation (within a factor of 2 of the prediction of equation 20) and, perhaps even more informatively, negligible systems lie beneath that line. Thus, according to these data, observed UWEs of above ∼1.4 could reliably be inferred to correspond to binary systems, and for a population the median properties of these

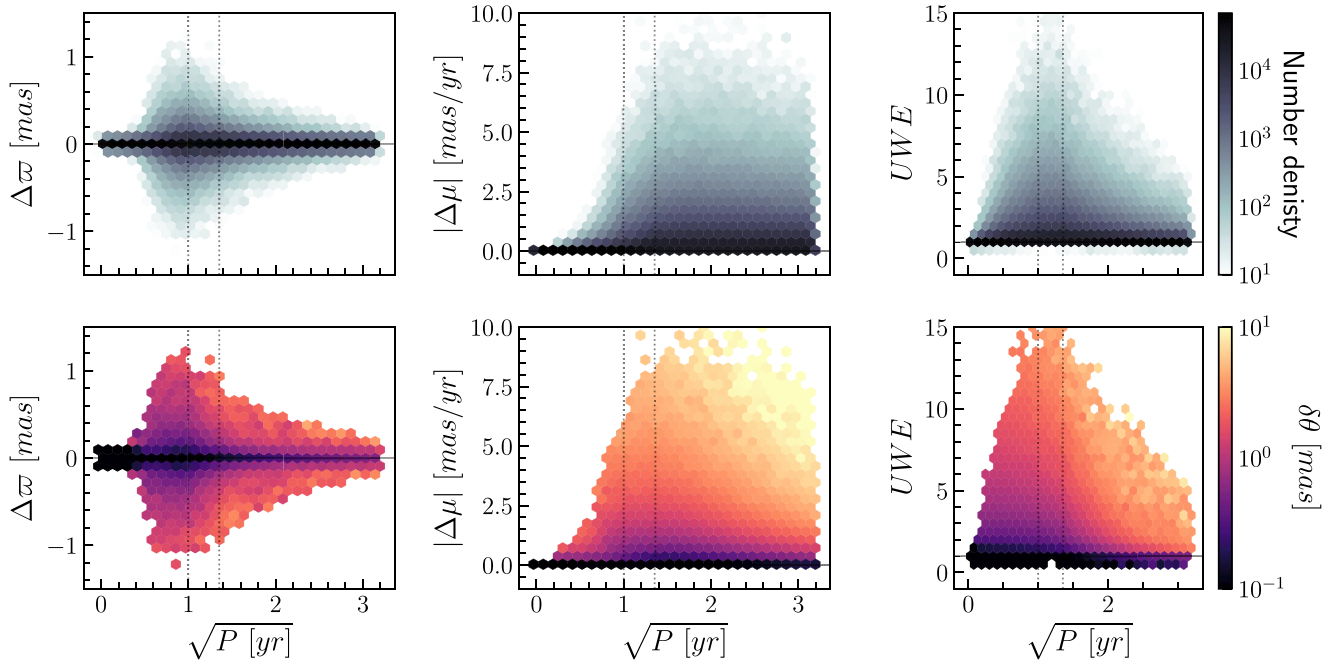

Figure 3. Comparison of the parallax and proper motion deviations, and the observed UWE, as a function of period. The x-axis is expressed as $\sqrt{P}$ such as to have uniform density of samples (see table 1). In the upper row, figures are coloured by number density, and in the lower by the median $\delta\theta$ that is a rough representation of the magnitude of the binary contribution. The vertical dashed lines show periods of 1 yr and of 22 months. We see that parallax is most affected by systems with a binary period of $\sim$1 yr, even if the effect of the binary is modest ($\delta\theta \lesssim 1$ mas). Proper motion can be affected by binaries of periods $\gtrsim$1 yr and the effect increases for more significant binary motion. Finally, the observed astrometric error, as expressed through the UWE, also peaks towards shorter periods, though less starkly than the parallax, and scales with the binary contribution.

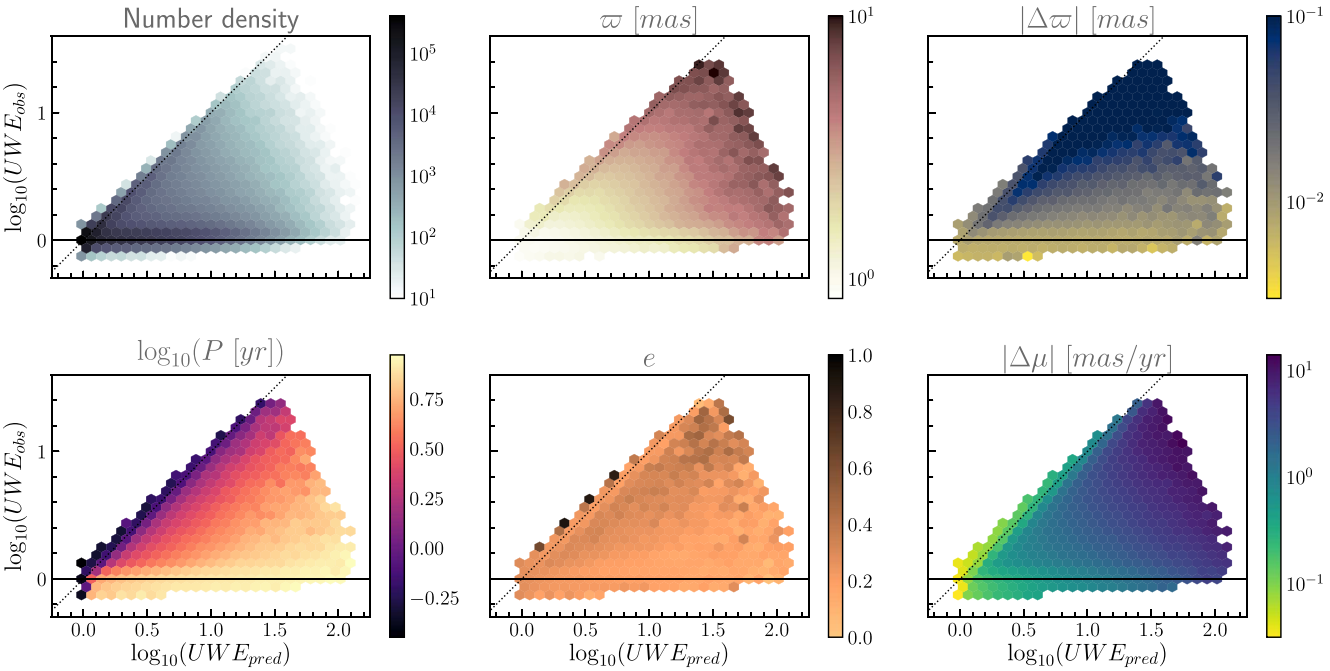

Figure 4. Comparison of the predicted UWE (via Section 2) and the UWE inferred from our mock observations. The dashed diagonal line shows a 1:1 correlation and the horizontal denotes an observed UWE of 1. Colour shows the median value of the specified parameter in each bin (save for the number density plot).

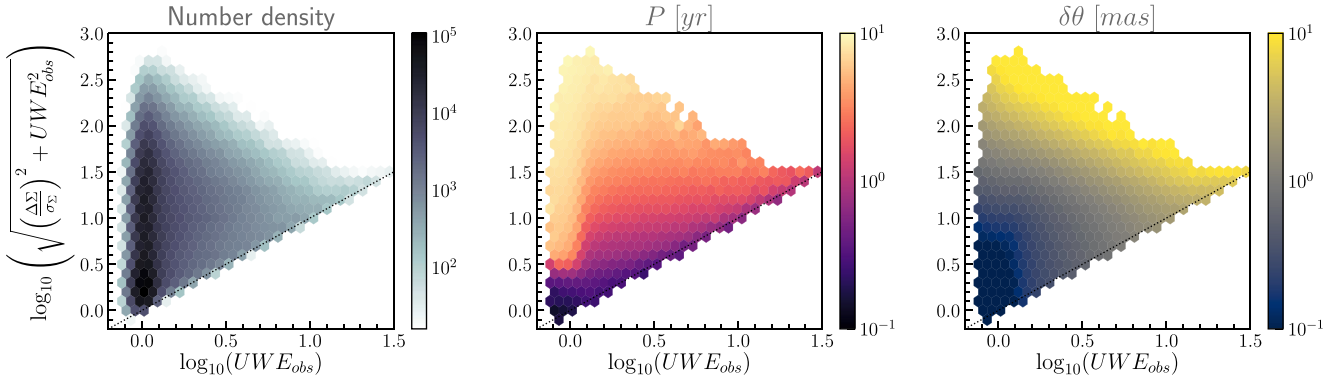

Figure 5. Comparison of the total variation (the sum of squares of all parameter deviations normalized by their errors) including UWE to the UWE alone. A 1:1 dotted line is shown for reference. Systems where most of the error is translated to UWE lie on or near this line, while others where significant binary motion has resulted in large deviations of the inferred parameters (but small corresponding UWE) are well above this line. We show the number density of all measurements, and the median period and $\delta\theta$.

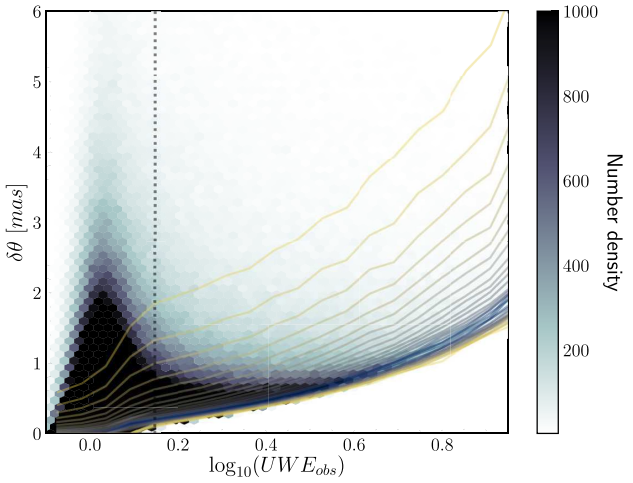

Figure 6. Comparison of the observed UWE to the true $\delta\theta$. Though the spread is large, above UWEs of around 1.4 (dotted line) there are negligible systems which do not contain a significant binary. For a given UWE (observable), we might ask whether we can constrain the binary properties. Confidence intervals of $\delta\theta$ for a given UWE are shown at 5 per cent intervals, ranging from 95 per cent (yellow) to 5 per cent (blue) – showing that we can predict with relatively confidence a value of $\delta\theta$ (within a factor of 2) but that the tail of the distribution skews to much higher values.

binaries can be well estimated. For an individual system, we can only make a probable estimate of $\delta\theta$, and there is always the possibility of a wild underestimate.

If the parallax is well constrained, $\delta\theta$ can be converted to a physical separation between the c.o.l. and c.o.m. If Δ can be estimated, this can be further translated to the true binary separation. Alternatively, if the period and phase are known, we can make a much more exact estimate of UWE for a given system (see Appendix B) and thus comparing to observations Δa can be precisely characterized.

This ignores any other sources of erroneous UWE that may exist in the data set – either due to systematic errors, occasional oddities, or other astrophysical sources. When applying this metric to real data sets, the precision of measurements of UWE will need to be tested explicitly to make inferences about individual objects. It may also be the case that other observed quantities, such as radial velocities or error on astrometric parameters (possibly including the covariances) can further help delineate and characterize binary systems.

5.2 Binary contamination

In Fig 7, we show the deviations and errors observed in our mock sample of two million binaries. Separating by period, $\delta\theta$, and $\mathrm{UWE_{obs}}$ illuminates which systems fill out the total distribution (black).

The largest panel shows the distribution of proper motion anomalies, with a clear bimodal behaviour – with mostly longer period systems having significant binary-induced proper motion, while for most short-period systems the proper motion signal is consistent with noise. A cut on UWE does not differentiate these two families, while a cut on $\delta\theta$ puts a strong upper limit on $\frac{|\Delta\mu|}{\sigma_\mu}$.

A UWE of 1.4 or below has been suggested as benchmark for removing binary contaminants. However, such a cut (yellow) still leaves around half of the binaries with $\delta\theta > 0.5$ and the majority of systems which have proper motion which have been skewed by multiple σ_μ. This sample does exclude the highest values of σ_ϖ and σ_μ, suggesting that they are well fitted, simply erroneously so. As we have stated before, this is the impact of binaries with periods a factor of a few times the observing period, for which the partial binary orbit mimics proper motion.

Smaller binaries, with lower values of $\delta\theta$ can still have significant UWE and cause large errors in parallax and proper motion. These account for almost all of the systems with a small $|\Delta\mu|$ and none of the systems with $|\Delta\mu| \gtrsim 10$. Shorter period binaries (red) can still have significant $\delta\theta$ and UWE, and as a population have the highest $|\Delta\varpi|$ (as we would expect given that this bracket covers the crucial 1 yr binary period). Significantly fewer of the high proper motion anomaly systems have short periods.

Before moving on from this plot, it is interesting to discuss how it would change if we had a longer observation interval. This would raise the period above which binary motion could be disguised as proper motion – narrowing the right-hand peak in $\frac{|\Delta\mu|}{\sigma_\mu}$ and moving it to higher values.

Denoting the fraction of all stars that are in binaries with periods less than 10 yr as ν, we can make some rough estimates for the

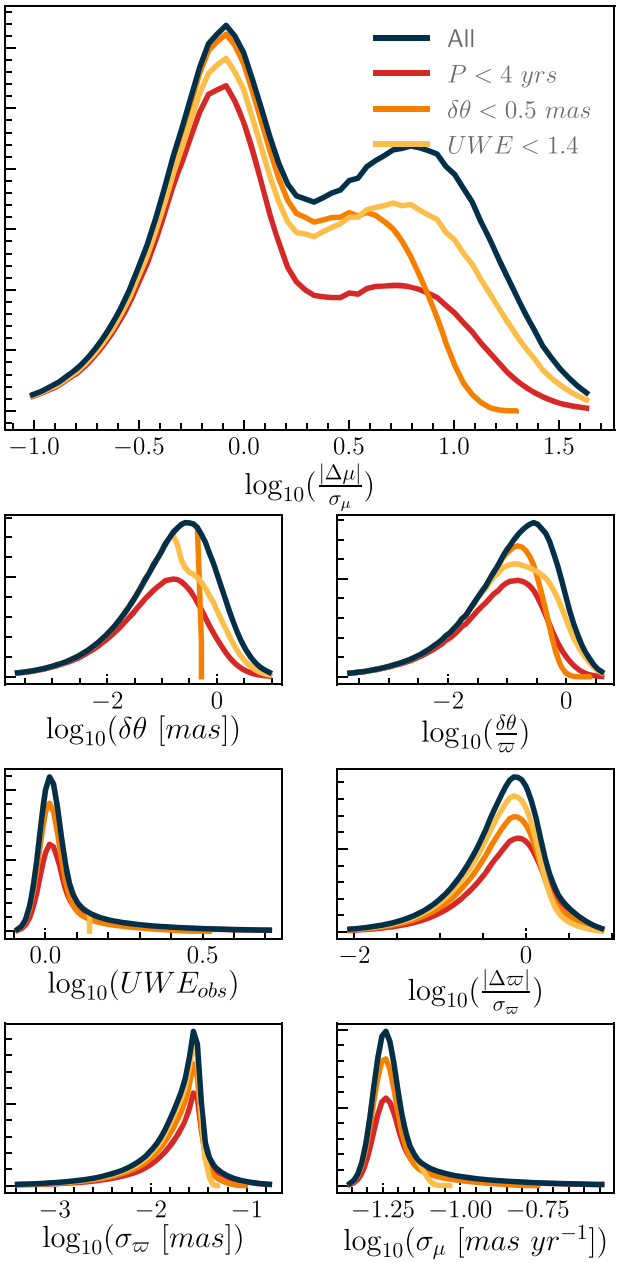

Figure 7. The distribution of our mock observations, as a function of the observed deviations and errors. As well as the total sample *(black)*, we show subsets with $\mathrm{UWE_{obs}} < 1.4$ *(yellow)*, $\delta\theta < 0.5$ mas *(orange)*, and $P < 4$ yr *(red)*. All *y*-scales are linear.

degree of binary dilution we should expect to see in astrometric samples, with UWE < 1.4 and

(i) $\delta\theta > 0.2$ mas: 30ν per cent
(ii) $\delta\theta > 1$ mas: 8ν per cent
(iii) $\Delta\varpi > \sigma_\varpi$: 20ν per cent
(iv) $\Delta\varpi > 0.1$ mas: 0.6ν per cent
(v) $\Delta\mu > 2\sigma_\mu$: 40ν per cent
(vi) $\Delta\mu > 1$ mas yr^{-1}: 4ν per cent.

This is of course dependent on survey length. Again, we are using *Gaia* DR2's 22 months here – longer baselines will lower these percentages, though they will also be able to detect deviations in systems with $P > 10$ yr.

Finally, it is interesting to focus on the subset of systems with periods close to 1 yr, which can well mimic parallactic motion over a binary orbit. Limiting ourselves to $0.9 < P[\mathrm{yr}] < 1.1$, the number of systems with $\Delta\varpi > 0.1$ mas goes up to 4ν per cent and we find that $\sim 0.01\nu$ per cent have $\Delta\varpi > 1$ mas.

UWE < 1.4 can still be a sensible and useful delimiter – but any such cut will let through a fraction of binaries, some of which will be significantly affected by their binarity. Depending on the case at hand, these may have little to no impact, or results may be skewed by either large numbers of small but significant binaries, or the very occasional extreme case. For example, though the shifts to ϖ are generally small, this measure is necessary to calculate the absolute magnitude of the star, and thus the most extreme binary contributions may change the inferred luminosity of a star significantly.

6 CONCLUSIONS

This paper has studied how unresolved binary systems will alter astrometric observations.

For shorter period binaries ($\lessapprox$ the observational baseline of the astrometric survey), the motion of the c.o.l. leads to increased error when fitting single body five-parameter astrometric solutions.[4] This excess error then provides a lower limit to the on-sky angular separation of the binary, which – assuming that the distance is well known – can be translated to physical separation and other binary properties. It is a lower limit, as there is always the possibility that some of the binary motion is translated into a shift from the true astrometric parameters (which describe the motion of the c.o.m. of the system), and thus the observed noise will be lower and the fit slightly biased. It is important to note that this ignores other sources of noise and confusion, and thus anomalously high astrometric error may be observed in single star systems – the reliability of this metric will depend on the instrument and quite likely the particular star. This means we can confidently make observations on a population level (when random noise will cancel out and astrometric bias will dilute our results but not mask them entirely), but inferences about individual systems will require very careful interpretation and may be impossible for many systems.

Longer period systems are more likely to bias the astrometric fit. Much of this bias is soaked up into excess proper motion (and position, but this is less physically meaningful). For systems with a period close to 1 yr, it may also cause the parallax to be under- or overestimated. This is less likely for eccentric orbits, for which the motion around their orbit is syncopated and thus is less easily mistaken for a parallactic ellipse. Periods significantly longer than the observational baseline (such that negligible orbital motion is observed) will just cause a constant offset of the position (thus binaries on 10+ yr orbits will have negligible impact on *Gaia* DR2).

All our analysis is limited to binary systems, though in theory much of this could be extended to systems with higher multiplicities. Depending on the scales, multiple systems may be well approximated as a binary (e.g. a hierarchical triple where a tight binary behaves analogously to a single star). As we are most sensitive to orbits with periods close to 1 yr, this may limit the multiplicity as

[4]Future *Gaia* data releases will include astrometric fits with >5 parameters (for a subset of stars) that will capture the binary motion described in this paper.

the more tightly packed a many-body system the more dynamically unstable it becomes.

We hope this work provides a window both into how astrometric observations may be affected by binaries, but also how binaries may be identified and in some case characterized from the discrepancy between their on-sky motion and a single-body astrometric fit. We explore this directly in Belokurov et al. (2020), in which we examine how UWE varies over the whole *Gaia* DR2 sample – identifying populations of systems that show signs of binarity and comparing to catalogues of known binaries and exoplanet hosts.

ACKNOWLEDGEMENTS

Special thanks to Simon Hodgkin, Emily Sandford, and all the members of the Cambridge Galactic Dynamics group. We thank Amanda Smith for the preparation of fig. 1. SK acknowledges the support by NSF grants AST-1813881 and AST-1909584 and Heising-Simons Foundation grant 2018-1030.

REFERENCES

Andrews J. J., Breivik K., Chatterjee S., 2019, ApJ, 886, 68
Bate M. R., Bonnell I. A., Price N. M., 1995, MNRAS, 277, 362
Belokurov V. et al., 2020, preprint (arXiv:2003.05467)
Bonnell I. A., Bate M. R., Zinnecker H., 1998, MNRAS, 298, 93
Duchêne G., Kraus A., 2013, ARA&A, 51, 269
Duquennoy A., Mayor M., 1991, A&A, 500, 337
El-Badry K., Rix H.-W., Ting Y.-S., Weisz D. R., Bergemann M., Cargile P., Conroy C., Eilers A.-C., 2018, MNRAS, 473, 5043
Gaia Collaboration, 2016, A&A, 595, A1
Gaia Collaboration, 2018, A&A, 616, A1
Hartman Z., Lépine S., 2020, AJ, 247, 66
Kervella P., Arenou F., Mignard F., Thévenin F., 2019, A&A, 623, A72
Kirk B. et al., 2016, AJ, 151, 68
Lindegren L. et al., 2016, A&A, 595, A4
Penoyre Z., Sandford E., 2019, MNRAS, 488, 4181
Perryman M. A. C. et al., 1997, A&A, 500, 501
Price-Whelan A. M. et al., 2020, preprint (arXiv:2002.00014)
Prša A. et al., 2011, AJ, 141, 83
Raghavan D. et al., 2010, ApJS, 190, 1
Sana H. et al., 2012, Science, 337, 444
Shahaf S., Mazeh T., Faigler S., Holl B., 2019, MNRAS, 487, 5610
Shu F. H., Adams F. C., Lizano S., 1987, ARA&A, 25, 23
Tutukov A. V., Yungelson L. R., 1981, Nauchnye Inf., 49, 3
Webbink R. F., 1984, ApJ, 277, 355
Whelan J., Iben I., Jr, 1973, ApJ, 186, 1007
Widmark A., Leistedt B., Hogg D. W., 2018, ApJ, 857, 114

APPENDIX A: THE C.O.L.

Finding the 'c.o.l.' of two objects is a similar, though much less well-defined exercise, to finding the c.o.m. It is only really a meaningful measure when the two (or more) sources are partially or completely unresolved, and has limited physical significance, being more a function of our observations than the behaviour of the system.

For point sources, and sufficiently small extended objects, objects will appear to have some finite width set by the resolving power of our instruments (and any additional sources of noise such as atmospheric turbulence) which here we will model as a Gaussian PSF – though a similar argument could be extended to any finite width symmetric distribution. We can model this as

$$b(x) \propto L\mathrm{e}^{-\frac{(x-\mu)^2}{2\sigma^2}}, \tag{A1}$$

where b is the surface brightness at some point x on sky (which can be measured in physical units or angular distances). L is the intrinsic luminosity of the source,[5] μ is the actual position of the source, and σ is the width of the PSF. Under the assumption that the PSF is mostly dependent on the instrument, not the source, σ should be a constant across similar observations, and for x measured in angle on sky, σ may be approximately constant for all observations. Though this is a one-dimensional distribution, the arguments can easily be extended to 2D.

We are mostly interested in pairs of unresolved sources, whose total brightness at some point along the line passing through both of their positions can be modelled as

$$b_\Sigma(x) \propto L_\mathrm{A} e^{-\frac{(x-\mu_\mathrm{A})^2}{2\sigma_A^2}} + L_\mathrm{B} e^{-\frac{(x-\mu_B)^2}{2\sigma_\mathrm{B}^2}}, \tag{A2}$$

where $(x-\mu_\mathrm{A}) \ll \sigma_A$ and $(x-\mu_\mathrm{B}) \ll \sigma_\mathrm{B}$ for x between μ_A and μ_B (i.e. between the two sources).

Thus, using the convention from Section 2.1 where $L = L_\mathrm{A}$ and $l = \frac{L_\mathrm{B}}{L_\mathrm{A}} < 1$

$$b_\Sigma(x) = L\left(1 + l - \frac{1}{2}\left(\frac{(x-\mu_\mathrm{A})^2}{2\sigma_\mathrm{A}^2} + \frac{(x-\mu_\mathrm{B})^2}{2\sigma_\mathrm{B}^2}\right)\right) + O(4). \tag{A3}$$

When this system is observed, it will appear to be a single source with a brightness $L' = L(1+l) + O(2)$ at a position μ' where $\frac{\mathrm{d}b_\Sigma}{\mathrm{d}x} = 0$. Thus,

$$\mu' = \frac{\mu_\mathrm{A} + \frac{l}{\epsilon^2}\mu_\mathrm{B}}{1 + \frac{l}{\epsilon^2}} + O(2), \tag{A4}$$

where $\epsilon = \frac{\sigma_\mathrm{B}}{\sigma_\mathrm{A}}$.

Working in coordinates such that $\mu_\mathrm{A} = 0$ (centred on the brighter object) and assuming that the PSF widths are the same for both objects (which is reasonable for two objects of comparable luminosity in a close binary – though may cause significant deviations in some cases), we recover the result from Section 2.1 describing the position of the c.o.l. of an unresolved binary:

$$\mu' = \frac{l\mu_\mathrm{B}}{1+l} + O(2). \tag{A5}$$

A1 1D scans instead of 2D images

The above argument assumes that we are free to orient the direction along which we measure the brightness of the source (and thus find the maximum) but that may not always be true – for example, the *Gaia* survey provides much more accurate astrometric measurements parallel to the direction it scans across the sky than perpendicular, and for dimmer sources it only records 1D positions.

If the system is scanned at an angle ϕ to the line connecting the two sources (where we can take ϕ to run from 0 to $\frac{\pi}{2}$ without loss of generality), then the measured c.o.l. position is modulated by a factor of $\cos\phi$. This means that for scans that only resolve perpendicular to the binary no c.o.l. motion is detected.

In general, we can assume that scan directions of the binary will be roughly isotropic and thus the observed c.o.l. shift will be

[5] In reality, the luminosity is spread over a spectrum of wavelengths and the observed brightness depends on the response function of our telescope. As we will be comparing observations made by a single instrument, we can think of L as already having taken the response function into account.

modulated by the average of $\cos\phi$ for $0 < \phi < \frac{\pi}{2}$ meaning observed displacements will be reduced by a factor of $\frac{2}{\pi}$.

In very particular cases, it is possible that the scans are aligned and timed such that an effectively stationary binary (i.e. one with a long period) appears to be moving significantly on sky and might be mistaken for other forms of motion. The frequency of such objects will be highly dependent on the form of the scanning law and a large degree of chance, but can be expected to be rare.

APPENDIX B: ANALYTIC SOLUTIONS FOR LONGER PERIOD BINARIES

The analytic deviations derived in Section 2 rely on the fact that the number of observed binary orbits is $\gtrsim$1, and thus the average over all time will tend to the average over a single orbit.

It is possible to perform the same analysis analytically (though requiring numerical integration) for any system provided the period and phase of the orbit at some point in time are known. For the vast majority of systems, this information is exactly what we would like to derive, and thus this analysis cannot be performed. However, for known binary systems where this information is available we could in theory use this to glean yet more insight into the system.

Let us first write out the trigonometric part of equation (15) in full

$$\boldsymbol{\epsilon} = \frac{\varpi\,\Delta a}{\Omega}\frac{1-e^2}{1+e\cos\eta}\begin{pmatrix}\cos\phi - \cos\psi_v\cos\phi_v\sin^2\theta_v\\ \sin\phi\cos\theta_v\end{pmatrix}, \tag{B1}$$

where

$$\Omega(\phi_v,\theta_v) = \sqrt{1-\cos^2\phi_v\sin^2\theta_v} \tag{B2}$$

is a constant throughout the orbit.

It will be useful to convert all time dependence [currently expressed in $\phi(t)$] in terms of η such that this becomes

$$\boldsymbol{\epsilon} = \frac{\varpi\,\Delta a}{\Omega}\begin{pmatrix}\Omega^2(\cos\eta - e) - \cos\phi_v\sin\phi_v\sin^2\theta_v\sqrt{1-e^2}\sin\eta\\ \sqrt{1-e^2}\sin\eta\cos\theta_v\end{pmatrix}. \tag{B3}$$

For a significant number of observations taken at uniform (or uniformly random) intervals between some t_1 and t_2 of a known binary with period P that passes through periapse at t_0 (which we will take to be the latest periapse passage before t_1), we can integrate this between η_1 and η_2 satisfying

$$t_1 - t_0 = \frac{P}{2\pi}(\eta_1 - e\sin\eta_1), \tag{B4}$$

which can be solved numerically (for η_2 we can perform the same calculation substituting t_1 for t_2).

Now we can find the time-averaged position via

$$\langle\boldsymbol{\epsilon}\rangle = \frac{1}{t_2-t_1}\int_{t_1}^{t_2}\boldsymbol{\epsilon}\,\mathrm{d}t = \frac{1}{\eta_2-\eta_1}\int_{\eta_1}^{\eta_2}(1-e\cos\eta)\boldsymbol{\epsilon}\,\mathrm{d}\eta; \tag{B5}$$

at this point it will be useful to define a family of integrals

$$I_{ab}(\eta_1,\eta_2) = \int_{\eta_1}^{\eta_2}\sin^a\eta\cos^b\eta. \tag{B6}$$

Letting $\Delta\eta = \eta_2 - \eta_1$ and $\Delta c_n = \cos(n\eta_2) - \cos(n\eta_1)$ (and similarly Δs_n for sines), we can write out all the terms needed for this calculation:

$$\begin{aligned}
I_{00} &= \Delta\eta\\
I_{10} &= -\Delta s_1\\
I_{01} &= \Delta c_1\\
I_{20} &= \frac{\Delta\eta}{2} - \frac{\Delta s_2}{4}\\
I_{11} &= -\frac{\Delta c_2}{4}\\
I_{02} &= \frac{\Delta\eta}{2} + \frac{\Delta s_2}{4}\\
I_{30} &= -\frac{3\Delta c_1}{4} + \frac{\Delta c_3}{12}\\
I_{21} &= \frac{\Delta s_1}{4} - \frac{\Delta s_3}{12}\\
I_{12} &= -\frac{\Delta c_1}{4} - \frac{\Delta c_3}{12}\\
I_{03} &= \frac{3\Delta s_1}{4} + \frac{\Delta s_3}{12}.
\end{aligned} \tag{B7}$$

Note that when $\Delta\eta$ is an integer multiple of 2π all terms except I_{00}, I_{20}, and I_{02} are 0 – hence the calculation is significantly easier if we integrate only over one full orbit. For arbitrary η_1 and η_2, these can take any value and must be pre-calculated (though for large $\delta\eta$, all trigonometric terms will be small, leading us back to the single orbit solution).

Performing the integral over time is thus simplified to the exercise of separating out powers of $\cos\eta$ and $\sin\eta$. This gives

$$\langle\boldsymbol{\epsilon}\rangle = \frac{\varpi\,\Delta a}{\Omega\Delta\eta}\begin{pmatrix}\Omega^2\zeta - \sin\phi_v\cos\phi_v\sin^2\theta_v\sqrt{1-e^2}(I_{10}-eI_{11})\\ \cos\theta_v\sqrt{1-e^2}(I_{10}-eI_{11})\end{pmatrix} \tag{B8}$$

and thus

$$\begin{aligned}
|\langle\boldsymbol{\epsilon}\rangle|^2 = \frac{\varpi^2\Delta^2a^2}{\Delta\eta^2}&(\Omega^2\zeta^2 - 2\sin\phi_v\cos\phi_v\sin^2\theta_v\sqrt{1-e^2}\\
&\times(I_{10}-eI_{11})\zeta + (1-\sin^2\phi_v\sin^2\theta_v)(I_{10}-eI_{11})^2),
\end{aligned} \tag{B9}$$

where

$$\zeta = (1+e^2)I_{01} - e(I_{00}+I_{02}) \tag{B10}$$

(which we have separated out only to keep the formulas from spilling out over many lines).

Performing the same analysis, we can find

$$\begin{aligned}
\langle|\boldsymbol{\epsilon}|^2\rangle = \frac{\varpi^2\Delta^2a^2}{\Delta\eta}\big(&I_{00}e^2 + I_{10}2e\sqrt{1-e^2}\sin\phi_v\cos\phi_v\sin^2\theta_v\\
&- I_{01}e(2+e^2)\Omega^2 + I_{20}(1-e^2)(1-\sin^2\phi_v\sin^2\theta_v)\\
&- I_{11}2(1+e^2)\sqrt{1-e^2}\sin\phi_v\cos\phi_v\sin^2\theta_v\\
&+ I_{02}(1+2e^2)\Omega^2 - I_{21}e(1-e^2)(1-\sin^2\phi_v\cos^2\theta_v)\\
&+ I_{12}2e\sqrt{1-e^2}\sin\phi_v\cos\phi_v\sin^2\theta_v - I_{03}e\Omega^2\big)
\end{aligned} \tag{B11}$$

and thus from equation (10) we can find $\delta\theta$ exactly.

In this regime, we can also find the proper motion anomaly, by averaging $\dot{\boldsymbol{\epsilon}}$ over $\Delta\eta$:

$$\langle\dot{\boldsymbol{\epsilon}}\rangle = \frac{1}{t_2-t_1}\int_{t_1}^{t_2}\dot{\boldsymbol{\epsilon}}\,\mathrm{d}t = \frac{\boldsymbol{\epsilon}(t_2)-\boldsymbol{\epsilon}(t_1)}{t_2-t_1}. \tag{B12}$$

It is interesting to note that while the leading order term of $\langle\boldsymbol{\epsilon}\rangle$ decays as $\Delta\eta^{-2}$ (and $\langle|\boldsymbol{\epsilon}|^2\rangle$ tends to a constant), the proper motion only decays as $\Delta\eta^{-1}$ on average – but will be zero for any orbit

harmonic with the observing period. Thus, even for large $\Delta\eta$ (many observed orbits) there may still be a significant bias on proper motion.

APPENDIX C: SINGLE BODY MOTION

The single body motion can be captured by considering the unit vector directed towards the source from the observer. If at some initial time, t_0, the source is at some on-sky position (azimuthal and polar angle) (α_0, β_0), and is moving with some proper motion (μ_α, μ_β), then at time t the unit vector from *Gaia* to the source obeys

$$\hat{\mathbf{r}} = \left\langle \hat{\mathbf{r_0}} + (t' - t_0)\left(\mu_\alpha \hat{\mathbf{p_0}} + \mu_\beta \hat{\mathbf{q_0}} + v_r \frac{\varpi}{A_u}\hat{\mathbf{r}}_\mathbf{0}\right) - \frac{\varpi}{A_u}\mathbf{b}(t')\right\rangle. \tag{C1}$$

The $< >$ brackets denote normalization, v_r is the radial velocity (which will disappear for all but the closest, fastest moving stars), and $t' = t - \frac{1}{c}(\mathbf{b}(t) - \mathbf{b}(t_0)) \cdot \hat{\mathbf{r}}_\mathbf{0}$ accounts for the slight variation in light traveltime due to Earth's orbit (at most a 16 min correction). $\mathbf{b}$ is the barycentric position of the satellite at time t and p is the parallax (i.e. it is this term that gives the epicycle-like motion of the source as viewed by *Gaia* and allows us to find the parallax) and A_u is one astronomical unit. Three orthogonal unit vectors describe the line-of-sight direction and those of increasing azimuthal and polar angle, respectively

$$\hat{\mathbf{r}}_\mathbf{0} = \begin{pmatrix} \cos\alpha_0 \cos\beta_0 \\ \sin\alpha_0 \cos\beta_0 \\ \sin\beta_0 \end{pmatrix}, \ \hat{\mathbf{p}}_\mathbf{0} = \begin{pmatrix} -\sin\alpha_0 \\ \cos\alpha_0 \\ 0 \end{pmatrix},$$
$$\hat{\mathbf{q}}_\mathbf{0} = \begin{pmatrix} -\cos\alpha_0 \sin\beta_0 \\ -\sin\alpha_0 \sin\beta_0 \\ \cos\beta_0 \end{pmatrix}. \tag{C2}$$

All angles and angular velocities are expressed in radians.

As $\hat{\mathbf{r}}$ gives the new approximate unit vector, we can find the azimuthal and polar angles at a given time via

$$\alpha(t) = \tan^{-1}\frac{\hat{r}_y}{\hat{r}_x} \ \text{ and } \ \beta(t) = \tan^{-1}\frac{\hat{r}_z}{\sqrt{\hat{r}_x^2 + \hat{r}_y^2}}. \tag{C3}$$

This expression ignores many (normally small) effects including evolution of the proper motions, either due to acceleration of the source or projection effects, as well as radial motion and relativistic time corrections. For our mostly qualitatively arguments it shall suffice, but a fuller description can be found in Lindegren et al. (2016).

In C1, we linearize these equations under the assumption that motion on sky is small to give a simpler approximate description of the motion.

C1 Linear model

The one-body astrometric motion (as expressed in equation C1) can be linearized in the limit of small on-sky motion. We can express the expected position of the object at time t as $\alpha(t) = \alpha_i + \Delta\alpha(t)$, where α_i is some initial reference position which the motion remains in the vicinity of. Similarly, $\beta(t) = \beta_i + \Delta\beta(t)$. Note that $\Delta\alpha_0 = \Delta\alpha(t_0)$ and similarly $\Delta\beta_0$ are not necessarily 0, accounting for the small offset caused by error and binary motion. We can assume that the deviations are small, except in edge cases with coordinate singularities but these can be avoided by a change of frame.

C1.1 Simplifying the barycentric position

It will be most convenient here to use coordinates aligned with the Earth's orbital plane (as it is motion in this plane that translates to the observed parallactic elliptical motion) and centred on the Sun. Thus, let α_i be the azimuthal angle covering $[0, 2\pi]$ and β_i the polar angle $[-\frac{\pi}{2}, \frac{\pi}{2}]$. In these coordinates, the position of the Earth at time t (and to a good approximation any observing instrument in Earth's orbit or at an Earth–Sun Lagrange point) is

$$\mathbf{b} = A_u(1 - e\sin\eta)\begin{pmatrix} \cos\Phi \\ \sin\Phi \\ 0 \end{pmatrix}, \tag{C4}$$

where e is the eccentricity (=0.0167), Φ is the phase of Earth's orbit, and η is the eccentric anomaly satisfying

$$\cos(\Phi) = \frac{\cos\eta - e}{1 - e\cos\eta}, \ \sin(\Phi) = \frac{\sqrt{1-e^2}\sin\eta}{1 - e\cos\eta} \tag{C5}$$

and

$$t - t_\mathrm{p} = \frac{T_\mathrm{E}}{2\pi}(\eta - e\sin\eta), \tag{C6}$$

where T_E is 1 yr and t_p is a reference time at which the Earth is at periapse.

In general, this last expression cannot be inverted, but in the limit of small eccentricity we can expand it to

$$\eta = \tau + e\sin\tau + O(2)\text{ , where } \tau = \frac{2\pi(t - t_\mathrm{p})}{T_\mathrm{E}}, \tag{C7}$$

which gives

$$\mathbf{b} = A_u\begin{pmatrix} \cos\tau - e(1 + \sin^2\tau) \\ \sin\tau + e\sin\tau\cos\tau \\ 0 \end{pmatrix}. \tag{C8}$$

C1.2 Linearized motion

The new normalized radial unit vector obeys

$$\hat{\mathbf{r}}(\alpha, \beta) = \hat{\mathbf{r}}_\mathbf{i} + \Delta\alpha\cos\beta_i\hat{\mathbf{p}}_\mathbf{i} + \Delta\beta\hat{\mathbf{p}}_\mathbf{i}, \tag{C9}$$

where $\hat{\mathbf{r}}_\mathbf{i}$, $\hat{\mathbf{p}}_\mathbf{i}$, and $\hat{\mathbf{q}}_\mathbf{i}$ are the equivalent of the vectors in equation (C2) evaluated at (α_i, β_i) and are all orthogonal.

As all deviations are small the new, non-normalized, radial vector accounting for the motion of the source is

$$\mathbf{r} = \hat{\mathbf{r}}_\mathbf{i} + (\Delta\alpha_0 + (t' - t_0)\mu_\alpha)\cos\beta_i\hat{\mathbf{p}}_\mathbf{i} + (\Delta\beta_0 + (t' - t_0)\mu_\beta)\hat{\mathbf{q}}_\mathbf{i} + v_r\frac{\varpi}{A_u}\hat{\mathbf{r}}_\mathbf{i} - \frac{\varpi}{A_u}\mathbf{b}(t') + O(2). \tag{C10}$$

All but the first term on the RHS are small and thus the magnitude of this vector is

$$|\mathbf{r}| = \sqrt{\mathbf{r}\cdot\mathbf{r}} = \sqrt{1 + 2\frac{\varpi}{A_u}(v_r - \mathbf{b}(t')\cdot\hat{\mathbf{r}}_\mathbf{i}) + O(2)} \tag{C11}$$

and thus the new radial unit vector can also be expressed as

$$\hat{\mathbf{r}} = \hat{\mathbf{r}}_\mathbf{i} + (\Delta\alpha_0 + (t' - t_0)\mu_\alpha)\cos\beta_i\hat{\mathbf{p}}_\mathbf{i} + (\Delta\beta_0 + (t' - t_0)\mu_\beta)\hat{\mathbf{q}}_\mathbf{i} + \frac{\varpi}{A_u}((\mathbf{b}(t')\cdot\hat{\mathbf{r}}_\mathbf{i})\hat{\mathbf{r}}_\mathbf{i} - \mathbf{b}(t')) + O(2). \tag{C12}$$

C1.3 Total linearized motion

Taking equations (C9) and (C12) and projecting in the $\hat{\mathbf{p}}_\mathbf{i}$ and $\hat{\mathbf{q}}_\mathbf{i}$ directions, we can express the on-sky motion of a single body

as

$$\Delta\alpha(t) = \Delta\alpha_0 + (t - t_0 - t_b)\mu_\alpha - \frac{\varpi}{\cos\beta_i}(\cos\psi + e(\sin\psi\sin\tau - \cos\phi)) \quad \text{(C13)}$$

and

$$\Delta\beta(t) = \Delta\beta_0 + (t - t_0 - t_b)\mu_\beta - \varpi\sin\beta_i(\sin\psi + e(\cos\psi\sin\tau + \sin\phi)), \quad \text{(C14)}$$

where

$$t_\mathrm{b} = \frac{A_u\cos\beta_i}{c}(\cos\psi - \cos\psi_0 + e(\sin\tau\sin\psi - \sin\tau_0\cos\psi_0)) \quad \text{(C15)}$$

and $\psi(t) = \Phi(t) - \tau$.

This shows the general form of parallactic motion – a linear translation from some initial displacement (e.g. the $\Delta\alpha_0 + \Delta t\mu_\alpha$ term in equation C13) and a circular motion projected on sky due to Earth's orbit (e.g. the $\varpi\sin\beta_i\sin\psi$ term in equation C14). The projection effect is stark, as polar motion due to parallax goes to zero near the ecliptic plane ($\beta_i \approx 0$) and azimuthal motion approaches a coordinate singularity at the poles (though changing to another frame of reference this behaviour disappears). This projection effect is the reason that it is much more difficult to determine parallaxes of objects on the ecliptic plane, only one component of the motion is visible, and thus the constraining power of the observations is reduced. The small factors of e and t_b slightly complicate this simple picture but only at the level of a few per cent; thus, intuition can still be gained from this linearized form.

APPENDIX D: FITTING TO MOCK OBSERVATIONS

To simulate observations, we can fit single-body astrometric solutions to the sample of generated mock observations.

Given the linearized version of the on-sky motion (equations C13 and C14), we can write the on-sky positions as

$$\begin{pmatrix}\boldsymbol{\alpha}_\mathrm{obs}\\ \boldsymbol{\beta}_\mathrm{obs}\end{pmatrix} = \mathbf{X}\boldsymbol{\pi} + \boldsymbol{\sigma}_\boldsymbol{\Sigma}, \quad \text{(D1)}$$

where $\boldsymbol{\sigma}_\boldsymbol{\Sigma}$ contains the error caused by the binary and by the random systematic astrometric error, normally distributed around zero with a width σ_ast.

We can calculate the best-fitting five-parameter astrometric model, $\hat{\boldsymbol{\pi}}$, via linear least squares:

$$\hat{\boldsymbol{\pi}} = \begin{pmatrix}\Delta\alpha_0\\ \Delta\beta_0\\ \mu_\alpha\\ \mu_\beta\\ \varpi\end{pmatrix} = \left(\mathbf{X}^T\mathbf{X}\right)^{-1}\mathbf{X}^T\begin{pmatrix}\boldsymbol{\alpha}_\mathrm{obs}\\ \boldsymbol{\beta}_\mathrm{obs}\end{pmatrix}, \quad \text{(D2)}$$

where $\boldsymbol{\alpha}_\mathrm{obs}$ and $\boldsymbol{\beta}_\mathrm{obs}$ are the vector of N_obs (=100) mock azimuthal and polar coordinates and

$$\mathbf{X}(\mathbf{t},\theta,\phi) = \begin{pmatrix}\mathbf{1}, & \mathbf{0}, & \mathbf{t} - \mathbf{t_b}(\mathbf{t},\theta,\phi), & \mathbf{0}, & \mathbf{p}_\alpha(\mathbf{t},\theta,\phi)\\ \mathbf{0}, & \mathbf{1}, & \mathbf{0}, & \mathbf{t} - \mathbf{t_b}(\mathbf{t},\theta,\phi), & \mathbf{p}_\beta(\mathbf{t},\theta,\phi)\end{pmatrix}, \quad \text{(D3)}$$

where

$$\mathbf{p}_\alpha(\mathbf{t},\theta,\phi) = -\frac{1}{\cos\theta}(\cos\boldsymbol{\psi} + e(\sin\boldsymbol{\tau}\sin\boldsymbol{\psi} - \cos\phi)) \quad \text{(D4)}$$

and

$$\mathbf{p}_\beta(\mathbf{t},\theta,\phi) = -\sin\theta(\sin\boldsymbol{\psi} + e(\sin\boldsymbol{\tau}\cos\boldsymbol{\psi} + \sin\phi)) \quad \text{(D5)}$$

[$\mathbf{0}$ and $\mathbf{1}$ are vectors of N_obs zeros and ones, respectively, $\mathbf{t}$ are the N_obs observing times, and $\boldsymbol{\psi}$ and $\boldsymbol{\tau}$ are the corresponding N_obs values of $\psi(t,\phi)$ and $\tau(t)$].

We can calculate the observed UWE as

$$\mathrm{UWE}_\mathrm{obs} = \frac{\left|\left|\begin{pmatrix}\boldsymbol{\alpha}_\mathrm{obs}\\ \boldsymbol{\beta}_\mathrm{obs}\end{pmatrix} - \mathbf{X}\hat{\boldsymbol{\pi}}\right|\right|}{\sigma_\mathrm{ast}\sqrt{N_\mathrm{obs} - 5}}. \quad \text{(D6)}$$

The corresponding errors in the parameters follow the 5 by 5 matrix

$$\hat{\boldsymbol{\sigma}}_\pi^2 = \sigma_\mathrm{ast}^2 \cdot \mathrm{UWE}_\mathrm{obs}^2(\mathbf{X}^T\mathbf{X})^{-1}, \quad \text{(D7)}$$

where the on-diagonal terms give us the variance on a single parameter and the off-diagonal terms the covariances. We will express approximate errors in the parameters as the square root of the on-diagonal terms.

APPENDIX E: PREDICTED VERSUS OBSERVED UWE BY PERIOD

Fig. E1 shows the predicted UWE compared to the observed value for binaries divided into three period intervals (separated at 2 and 5 yr). Now we can see very clearly the high good agreement between predictions and the mock observations for short-period systems. Even for periods a few times longer than the observing baseline (22 months), the observed UWE can be large.

Here we can see clearly that highly eccentric orbits, even on long periods, can have large observed UWE – as though only part of the orbit is resolved if that fraction overlaps with the fast motion through periapse passage we still capture much of the total orbital motion.

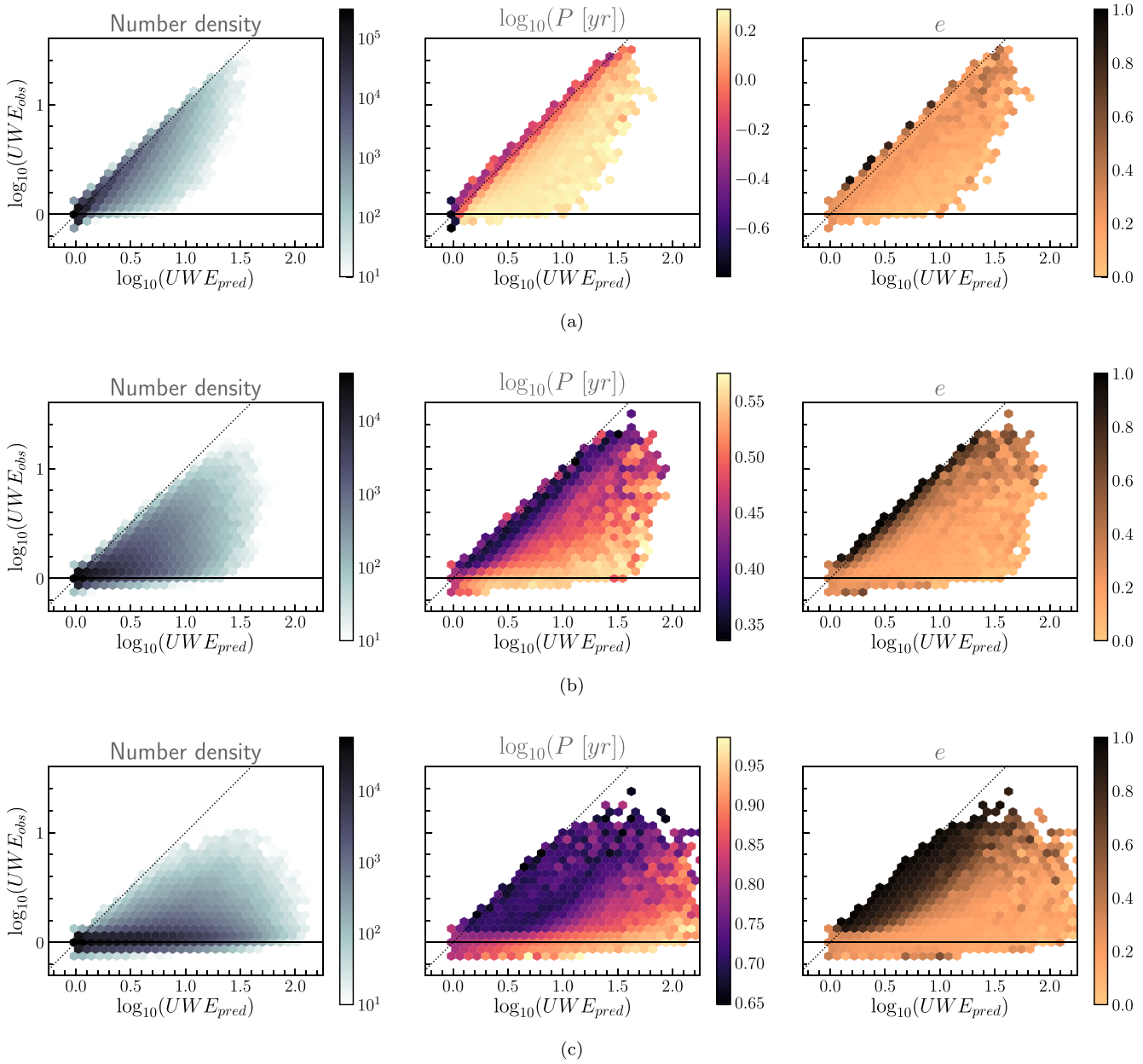

Figure E1. Predicted versus observed UWE (as in Fig. 4) from our mock observations, separated by period of binary orbit. Top: $P < 2$ yr, Middle: 2 yr $< P < 5$ yr and bottom: $P > 5$ yr. Note the changing scale of the colour bar for the median periods.

This paper has been typeset from a TEX/LATEX file prepared by the author.